PHYSICAL REVIEW E **102**, 063302 (2020)

Spectroscopic analysis in molecular simulations with discretized Wiener-Khinchin theorem for Fourier-Laplace transformation

Akira Koyama [*]
Department of General Education, National Institute of Technology, Toyota College, 2-1 Eisei-cho, Toyota, Aichi 471-8525, Japan

David A. Nicholson, Marat Andreev, and Gregory C. Rutledge
Department of Chemical Engineering, Massachusetts Institute of Technology, 77 Massachusetts Avenue, Cambridge, Massachusetts 02139, USA

Koji Fukao
Department of Physical Sciences, Ritsumeikan University, Kusatsu, Shiga 525-8577, Japan

Takashi Yamamoto
Department of Physics and Informatics, Yamaguchi University, Yamaguchi 753-8512, Japan

(Received 5 June 2020; accepted 7 October 2020; published 9 December 2020)

The Wiener-Khinchin theorem for the Fourier-Laplace transformation (WKT-FLT) provides a robust method to obtain the single-side Fourier transforms of arbitrary time-domain relaxation functions (or autocorrelation functions). Moreover, by combining an on-the-fly algorithm with the WKT-FLT, the numerical calculations of various complex spectroscopic data in a wide frequency range become significantly more efficient. However, the discretized WKT-FLT equation, obtained simply by replacing the integrations with the discrete summations, always produces two artifacts in the frequency-domain relaxation function. In addition, the artifacts become more apparent in the frequency-domain response function converted from the relaxation function. We find the sources of these artifacts that are associated with the discretization of the WKT-FLT equation. Taking these sources into account, we derive discretized WKT-FLT equations designated for both the frequency-domain relaxation and response functions with the artifacts removed. The use of the discretized WKT-FLT equations with the on-the-fly algorithm is illustrated by a flow chart. We also give application examples for the wave-vector-dependent dynamic susceptibility in an isotropic amorphous polyethylene and the frequency-domain response functions of the orientation vectors in an *n*-alkane crystal.

DOI: 10.1103/PhysRevE.102.063302

I. INTRODUCTION

The Wiener-Khinchin theorem (WKT) [1,2] is a well-known general-purpose method to obtain Fourier transforms of arbitrary autocorrelation functions (ACFs) by computing the power spectral density. The theorem states that the power spectral density of a time series of a variable in a stationary state always exists even when the time series is neither absolutely integrable nor square integrable, and that the power spectral density coincides with the Fourier transform of the ACF. Originally, the WKT was developed and used to analyze data obtained from linear time-invariant systems constructed as electric circuits [3]. Today, the theorem plays important roles in various fields of signal processing and analysis.

In the fields of materials science and technology, the WKT is deeply connected with the fluctuation-dissipation theorem [4,5] and linear-response theory [6–8], and it contributes for the construction of stationary-state nonequilibrium physics and chemistry [9] as an essential tool. These theoretical approaches are widely used to investigate the dynamics observed in materials both experimentally and numerically. Recently, the WKT itself is also applied to obtain the Fourier transforms of ACFs and to investigate the molecular processes in numerical simulations. Based on developments in parallel computation tools such as multithreading, message-passing interfaces, general-purpose GPU calculations, and supported by high-performance solid-state memory devices, numerically computed spectroscopic data are now comparable to experimental data [10–16]. Some such data were computed by using the WKT instead of by the direct Fourier transformation for the ACFs. Here we show the outline of how to use the WKT in the molecular simulations.

Given a physical quantity $f(t)$ as a function of time t, the ACF is

$$F(t) \equiv \frac{\langle f(t) f(0)\rangle}{\langle f(0) f(0)\rangle} = \frac{1}{A}\langle f(t+t_0) f(t_0)\rangle_{t_0}, \tag{1}$$

where $\langle\cdots\rangle$ means the statistical average and A is a normalization factor. By assuming an ergodic system, we replace the statistical average $\langle\cdots\rangle$ with a long-time average $\langle\cdots\rangle_{t_0}$ over t_0 [9].

---

[*] koyama@toyota-ct.ac.jp

Both in deterministic and stochastic cases, *the WKT equation* is written as the following relation:

$$F(\omega) = I(\omega), \tag{2}$$

where ω is an angular frequency, $F(\omega)$ is the Fourier transform of the ACF $F(t)$, and $I(\omega)$ is the power spectral density of the physical quantity of $f(t)$. The functions $F(\omega)$ and $I(\omega)$ are defined as follows:

$$F(\omega) \equiv \int_{-\infty}^{\infty} F(t)\, e^{i\omega t}\, dt \tag{3}$$

and

$$I(\omega) \equiv \frac{1}{A} \lim_{T\to\infty} \frac{1}{T} \left| \int_{-T/2}^{T/2} f(t)\, e^{i\omega t}\, dt \right|^2, \tag{4}$$

where T is a time interval. The WKT equation is interpreted as follows: *the Fourier transform of the ACF $F(t)$ is proportional to the product of the Fourier transform of $f(t)$ and its complex conjugate*. In the literature on molecular simulations, the WKT equation is often written in the following form for simplicity [11,15]:

$$F(\omega) = \frac{1}{A} \lim_{T\to\infty} \frac{1}{T} \left| \int_{-T/2}^{T/2} f(t)\, e^{i\omega t}\, dt \right|^2. \tag{5}$$

To use the WKT in molecular simulations, the continuous WKT equation (5) must be discretized. By replacing the continuous ω with a discrete $\omega_n = 2\pi n/T$, we remove the notation for the operation $\lim_{T\to\infty}$ (hereafter, we refer to the $\lim_{T\to\infty}$ as 'the limit on T') from Eq. (5) and replace the integrals with discrete summations. As a result, we get the discretized WKT equation as follows:

$$\begin{aligned} F(\omega_n) &= \frac{1}{AT} \left\langle \left| \sum_{m=-M/2+1}^{M/2} \Delta t\, f(t_m)\, e^{i\omega_n t_m} \right|^2 \right\rangle \\ &= \frac{\Delta t}{AM} \langle\, |f(\omega_n)|^2\, \rangle, \end{aligned} \tag{6}$$

where m, n, and M are integers, and Δt is a time mesh. Because the limit on T has been removed from Eq. (5), we add the brackets of the statistical average $\langle \cdots \rangle$ to Eq. (6). When we actually compute $F(\omega_n)$, we replace the statistical average $\langle \cdots \rangle$ with the average over the number of simulations performed under the same thermodynamic and computational conditions. The discretized Fourier transformation for $f(t_m)$ is written as

$$f(\omega_n) = \sum_{m=-M/2+1}^{M/2} f(t_m)\, e^{i\omega_n t_m}. \tag{7}$$

In Eqs. (6) and (7), the variables and constants are

$$\begin{gathered} t_m = m\Delta t,\ -M/2+1 \leqslant m \leqslant M/2,\ M \text{ is even}, \\ \omega_n = n\Delta\omega,\ \Delta\omega = \frac{2\pi}{M\Delta t},\ 1 \leqslant n \leqslant M/2, \text{ and} \\ T = M\Delta t, \end{gathered} \tag{8}$$

where the range of n is half that of m because of the Nyquist-Shannon sampling theorem [3,17], and the maximum value of $\omega_n = \pi/\Delta t$ is the Nyquist frequency. The constant $\Delta\omega$ gives the lower resolution limit of $F(\omega_n)$. By using the discretized WKT equation, we can compute the Fourier transform $F(\omega_n)$ of the ACF, which is called the "frequency-domain correlation (or relaxation) function," from molecular simulations.

For example, density, mass flow, stress, or other physical quantities are functions of time in molecular simulations and can be written as $f(t_m)$ in Eqs. (6) and (7). If we have the complete time series $f(t_m)$ in computer storage, we can apply the discrete Fourier transformation of Eq. (7) to get the Fourier components $f(\omega_n)$. According to Eq. (6), multiplying $f(\omega_n)$ by its complex conjugate gives the frequency-domain correlation functions of density, mass flow, stress, and other physical quantities, without computing their ACFs and without implementing the direct Fourier transformation for the ACFs. The WKT provides a much easier way to obtain $F(\omega_n)$.

However, the WKT has its limitations. The function $F(\omega_n)$ computed by using the WKT is always a real function because the ACF is a real, even function of time. Experimental data of spectroscopic measurements often have the imaginary part together with the real part; the former is related to energy loss, and the latter to energy stored. The complex frequency-domain correlation function is given by the Fourier-Laplace transformation (a single-side Fourier transformation) for the ACF, instead of by the Fourier transformation [Eq. (3)], which is written as

$$F^{+}(\omega) \equiv \int_{0}^{\infty} F(t)\, e^{i\omega t}\, dt, \tag{9}$$

where the superscript $+$ $(-)$ indicates that the interval of integration on the right-hand side is positive (negative). Of course, the imaginary part can be obtained analytically from the real part by using the Kramers-Kronig relation [9], but this is difficult to do numerically. To obtain the imaginary parts from the simulations, we should modify and extend the usual WKT.

Matsui and co-workers presented an extended WKT equation for the Fourier-Laplace transformation (WKT-FLT) to compute complex dynamic structure factor and complex dielectric constant from molecular dynamics (MD) simulations [18–20]. In addition, to compute the spectra in a wide frequency range, they combined an on-the-fly algorithm for implementing the WKT-FLT with thinning out the angular frequency ω_n (see Appendix A for details).

Their strategy is robust and is attractive in many research fields, not only in materials physics but also in molecular chemistry and biology. However, when we discretize their WKT-FLT equation simply by replacing the integrations with the summations as done from Eq. (5) to (6), the discretized equation always produces two artifacts in $F^{+}(\omega_n)$. In addition, the artifacts become more apparent in the "frequency-domain response function" $\chi^{+}(\omega_n)$ (often called the "dynamic susceptibility"), which is converted from $F^{+}(\omega_n)$ by using [9]

$$\chi^{+}(\omega) = 1 + i\omega F^{+}(\omega). \tag{10}$$

Figure 1 presents the artifacts observed in $F^{+}(\omega_n)$ and $\chi^{+}(\omega_n)$ for the bisect vectors $\mathbf{u}_j^{\vdash}(t)$ [illustrated in Fig. 1(a)] of the united atom polyethylene model at 500 K (a melting

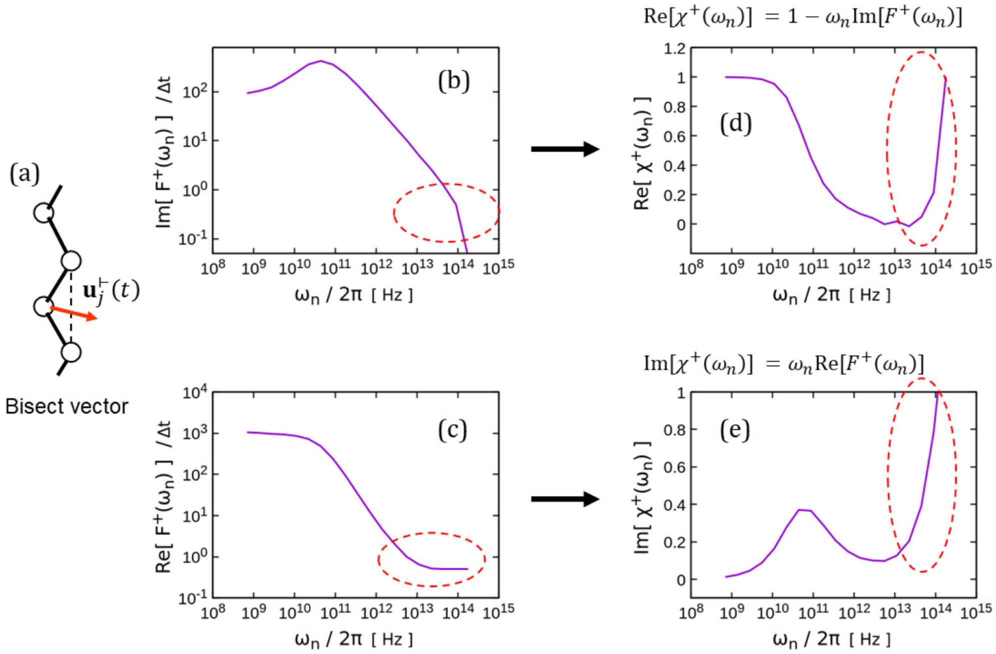

FIG. 1. Artifacts observed in $F^+(\omega_n)$ and $\chi^+(\omega_n)$ for the bisect vectors $\mathbf{u}_j^{\perp}(t)$ [illustrated in panel (a)] of the united atom polyethylene model at 500 K (a melting state), computed by using the WKT-FLT equation from molecular dynamics (MD) simulations. In the left column, panels (b) and (c) show the imaginary part and the real part of $F^+(\omega_n)$ plotted versus $\log \omega_n$, respectively. In the right column, panels (d) and (e) are the real part and the imaginary part of $\chi^+(\omega_n)$ converted from $F^+(\omega_n)$ by using $\chi^+(\omega) = 1 + i\omega F^+(\omega)$ [Eq. (10)]. The parts indicated by dashed red ellipses are the artifacts. In the left column, the upper curve should approach the asymptotic curve of $1/\omega_n$, and the lower curve should converge to zero, but they do not. The artifacts result in the strange increase in $\chi^+(\omega_n)$ for large ω_n.

state), computed by using the WKT-FLT equation from MD simulations (see Appendix F 1 for the simulation outline).

In Figs. 1(d) and 1(e), both the real and imaginary parts of $\chi^+(\omega_n)$ are expected to converge to zero as ω_n increases. Thus, the imaginary part of $F^+(\omega_n)$ [Fig. 1(b)] should asymptotically approach $1/\omega_n$, and the real part of $F^+(\omega_n)$ [Fig. 1(c)] should converge to zero with increasing ω_n. However, this does not happen: $\mathrm{Im}[F^+(\omega_n)]$ deviates from $1/\omega_n$, and $\mathrm{Re}[F^+(\omega_n)]/\Delta t$ converges to $1/2$ for large ω_n. The sources of this undesirable behavior remain unknown. Therefore, the goals of this study are the following:

(1) To clarify the sources of the artifacts and
(2) To remove the artifacts.

The on-the-fly algorithm combined with the thinning-out for the angular frequency ω_n is significantly useful and essential for computing the spectra in a wide frequency range. However, this algorithm was explained very briefly in the original papers [18–20]. For the benefit to easily be understood, we explain it in Appendix A using the WKT [Eqs. (6)–(8)]. We recommend seeing Appendix A in advance for the readers who are interested in the algorithm.

Depending on the research field, numerous names exist for the functions $F(t)$, $\chi(t)$, $F^+(\omega)$, and $\chi^+(\omega)$. To avoid confusion, we call $F(t)$ and $\chi(t)$ the time-domain relaxation function and response function, respectively, and we call their Fourier-Laplace transforms $F^+(\omega)$ and $\chi^+(\omega)$ the frequency-domain relaxation function and response function, respectively. The relaxation function is also referred to the correlation function, so we use the term "correlation" instead of relaxation if appropriate. In the time domain, we mainly deal with ACFs. Thus, in most cases, we call $F(t)$ the ACF.

II. EFFECTIVE AUTOCORRELATION FUNCTION

First, we derive an effective ACF for the WKT, which will be an important tool throughout this research.

Suppose that a quantity $f(t)$ of interest is a function of time t, then we define a long-time-averaged ACF $F(t)$ of $f(t)$ as

$$\begin{aligned} F(t) &\equiv \frac{1}{A}\langle f(t+t_0)f(t_0)\rangle_{t_0} \\ &= \frac{1}{A}\lim_{T\to\infty}\frac{1}{T}\int_{-T/2}^{T/2} dt_0\; f(t+t_0)f(t_0). \end{aligned} \tag{11}$$

The constant A is a normalization factor defined as

$$\begin{aligned} A &\equiv \langle f(t_0)f(t_0)\rangle_{t_0} \\ &= \lim_{T\to\infty}\frac{1}{T}\int_{-T/2}^{T/2} dt_0\; f(t_0)f(t_0). \end{aligned} \tag{12}$$

Here we assume that the time series of f is computed from a molecular simulation limited to a finite time interval from $-T/2$ to $T/2$, and we use this f for Eq. (11) after removing the limit on T. In this case, both $f(t+t_0)$ and $f(t_0)$ in Eq. (11) become restricted to the same time interval as the simulation. With this assumption, we restrict the domain of $f(t+t_0)$ to $-T/2 < t + t_0 < T/2$ as follows:

$$f(t+t_0) = \int_{-T/2}^{T/2} dt'\, f(t')\, \delta(t' - (t+t_0)), \tag{13}$$

where $\delta(t)$ is the Dirac δ function. On substituting Eq. (13) into Eq. (11), we obtain the following form of *the effective ACF* $F_{\mathrm{e}}(t)$:

$$\begin{aligned} F(t) &\cong F_{\mathrm{e}}(t) \\ &= \frac{1}{A}\lim_{T\to\infty}\frac{1}{T}\int_{-T/2}^{T/2} dt_0 \\ &\quad\times \int_{-T/2}^{T/2} dt' f(t')f(t_0)\,\delta(t'-(t+t_0)). \end{aligned} \tag{14}$$

Integrating Eq. (14) over t' or t_0 with the cases $t' > t_0$ and $t' < t_0$, we see that $F_{\mathrm{e}}(t)$ is an even function: $F_{\mathrm{e}}(t) = F_{\mathrm{e}}(-t)$.

The usual WKT equation is derived by using the effective ACF $F_{\mathrm{e}}(t)$. Substituting $F_{\mathrm{e}}(t)$ [Eq. (14)] into the right-hand side of Eq. (3) instead of $F(t)$ [Eq. (11)] gives

$$\begin{aligned} F(\omega) &= \int_{-\infty}^{\infty} F_{\mathrm{e}}(t)\, e^{i\omega t}\, dt \\ &= \frac{1}{A}\lim_{T\to\infty}\frac{1}{T}\int_{-T/2}^{T/2} dt_0 \int_{-T/2}^{T/2} dt'\; f(t')f(t_0) \\ &\quad\times \int_{-\infty}^{\infty} dt\; e^{i\omega t}\;\delta(t'-(t+t_0)) \\ &= \frac{1}{A}\lim_{T\to\infty}\frac{1}{T}\int_{-T/2}^{T/2} dt_0 \\ &\quad\times \int_{-T/2}^{T/2} dt' f(t')f(t_0)\, e^{i\omega(t'-t_0)}. \end{aligned} \tag{15}$$

We then obtain the WKT equation, which is the same as Eq. (5):

$$\begin{aligned} F(\omega) &= \int_{-\infty}^{\infty} F_{\mathrm{e}}(t)\, e^{i\omega t}\, dt \\ &= \frac{1}{A}\lim_{T\to\infty}\frac{1}{T}\left|\int_{-T/2}^{T/2} f(t)\, e^{i\omega t}\, dt\right|^2. \end{aligned} \tag{16}$$

Note that the effective ACF $F_{\mathrm{e}}(t)$ does not correspond exactly to $F(t)$ [Eq. (11)] as indicated by the notation $\cong$ in Eq. (14). The integration area of Eq. (14) on the t' versus t_0 plane differs from that of Eq. (11). See Appendixes B and C for details.

III. WKT-FLT EQUATION FOR RELAXATION FUNCTION

This section derives a WKT-FLT equation with the effective ACF $F_{\mathrm{e}}(t)$.

Introducing the Heaviside unit step function $\theta(t)$ into Eq. (9), $F^{+}(\omega)$ becomes

$$F^{+}(\omega) = \int_{0}^{\infty} F(t)\, e^{i\omega t}\, dt = \int_{-\infty}^{\infty} \theta(t)\, F(t)\, e^{i\omega t}\, dt, \tag{17}$$

where

$$\theta(t) \equiv \left\{ \begin{array}{ll} 1, & t>0 \\ 1/2, & t=0 \\ 0, & \text{otherwise} \end{array} \right\}. \tag{18}$$

Note that the unit step function $\theta(t)$ is neither even nor odd. Thus, $\theta(t)F(t)$ in the integrand of Eq. (17) is also neither even nor odd. In Eq. (18), we set $\theta(0) = 1/2$ to satisfy the sum rules described later. Substituting the effective ACF $F_{\mathrm{e}}(t)$ [Eq. (14)] into Eq. (17) instead of $F(t)$ [Eq. (11)], we obtain

$$\begin{aligned} F^{+}(\omega) &= \int_{-\infty}^{\infty} \theta(t) F_{\mathrm{e}}(t)\, e^{i\omega t}\, dt \\ &= \frac{1}{A}\lim_{T\to\infty}\frac{1}{T}\int_{-T/2}^{T/2} dt_0 \int_{-T/2}^{T/2} dt'\; f(t')f(t_0) \\ &\quad\times \int_{-\infty}^{\infty} dt\; \theta(t)\, e^{i\omega t}\;\delta(t'-(t+t_0)) \\ &= \frac{1}{A}\lim_{T\to\infty}\frac{1}{T}\int_{-T/2}^{T/2} dt_0 \\ &\quad\times \int_{-T/2}^{T/2} dt'\; f(t')f(t_0)\,\theta(t'-t_0)\, e^{i\omega(t'-t_0)}. \end{aligned} \tag{19}$$

We then get *the WKT-FLT equation for the relaxation function*:

$$\begin{aligned} F^{+}(\omega) &= \int_{0}^{\infty} F_{\mathrm{e}}(t)\, e^{i\omega t}\, dt \\ &= \frac{1}{A}\lim_{T\to\infty}\frac{1}{T}\int_{-T/2}^{T/2} dt_0\, f(t_0)\, e^{-i\omega t_0}\int_{t_0}^{T/2} dt' f(t')\, e^{i\omega t'}. \end{aligned} \tag{20}$$

Equation (20) is the same as the existing WKT-FLT equation [19], although the ways of the derivations differ.

Next, we examine the WKT-FLT equation in detail. Introducing the unit step function $\theta(-t)$, $F^{-}(\omega)$ is written as

$$F^{-}(\omega) = \int_{-\infty}^{0} F(t)\, e^{i\omega t}\, dt = \int_{-\infty}^{\infty} \theta(-t)\, F(t)\, e^{i\omega t}\, dt. \tag{21}$$

In the same way as we derived Eq. (20), we get $F^{-}(\omega)$:

$$\begin{aligned} F^{-}(\omega) &= \int_{-\infty}^{0} F_{\mathrm{e}}(t)\, e^{i\omega t}\, dt \\ &= \frac{1}{A}\lim_{T\to\infty}\frac{1}{T}\int_{-T/2}^{T/2} dt_0\, f(t_0)\, e^{-i\omega t_0}\int_{-T/2}^{t_0} dt' f(t')\, e^{i\omega t'}. \end{aligned} \tag{22}$$

If we switch the order of the integrals in Eq. (22), switch the variables t' and t_0, and take the complex conjugate, we see that

$$F^{+}(\omega) = (F^{-}(\omega))^{*}, \tag{23}$$

where the notation $*$ means the complex conjugate. Combining Eqs. (20) and (22) gives

$$F(\omega) = F^{+}(\omega) + F^{-}(\omega), \tag{24}$$

where $F(\omega)$ is the Fourier transform of the ACF given in Eq. (5). Figure 2 shows the integration areas of $F^{+}(\omega)$ and $F^{-}(\omega)$ on the t' versus t_0 plane.

Even when integrating both sides of Eq. (24) over ω, we still obtain

$$\int_{-\infty}^{\infty} d\omega\; F(\omega) = \int_{-\infty}^{\infty} d\omega\; F^{+}(\omega) + \int_{-\infty}^{\infty} d\omega\; F^{-}(\omega), \tag{25}$$

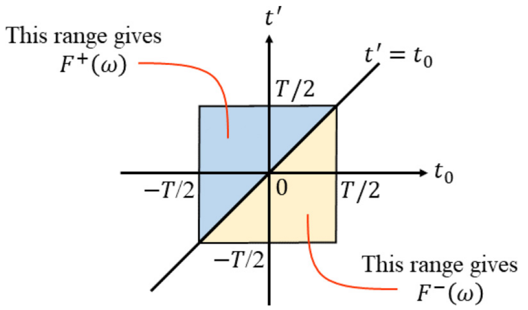

FIG. 2. Integration area of $F^+(\omega)$ and $F^-(\omega)$ over the t' versus t_0 plane.

because the sum rules for $F(\omega)$, $F^+(\omega)$, and $F^-(\omega)$ are

$$\int_{-\infty}^{\infty} d\omega\; F(\omega) = \int_{-\infty}^{\infty} d\omega \int_{-\infty}^{\infty} dt\; F(t)\, e^{i\omega t} = 2\pi F(t=0) \tag{26}$$

and

$$\int_{-\infty}^{\infty} d\omega\; F^{\pm}(\omega) = \int_{-\infty}^{\infty} d\omega \int_{-\infty}^{\infty} dt\; \theta(\pm t)\, F(t)\, e^{i\omega t} = \pi F(t=0), \tag{27}$$

where the Dirac δ function is

$$\delta(t) = \int_{-\infty}^{\infty} \frac{d\omega}{2\pi} e^{i\omega t}. \tag{28}$$

Equation (25) holds because we set $\theta(0) = 1/2$. Otherwise, the right-hand side of Eq. (27) is not $\pi F(t=0)$, which invalidates Eq. (25). For Eq. (24) to safely hold, including the case of Eq. (25), we must define the unit step function as done in Eq. (18).

IV. DISCRETIZED WKT-FLT EQUATION FOR RELAXATION FUNCTION AND A CORRECTION TERM FOR OVERCOUNTING

In this section, we discretize the WKT-FLT equation and show that the discretized version must include a correction term to eliminate an overcounting.

Replacing the continuous ω with the discrete $\omega_n = 2\pi n/T$ and removing the limit on T from Eq. (20) gives

$$F^+(\omega_n) = \frac{1}{AT}\left\langle \int_{-T/2}^{T/2} dt_0\, f(t_0)\, e^{-i\omega_n t_0} \int_{t_0}^{T/2} dt'\, f(t')\, e^{i\omega_n t'} \right\rangle, \tag{29}$$

where the right-hand side of Eq. (29) is enclosed in the brackets $\langle\cdots\rangle$. Because the statistical average is replaced with the long-time average when assuming ergodicity, we add the statistical-average brackets back to the equation when the limit on T is removed. Again including the unit step function $\theta(t)$, we rewrite Eq. (29) in the form

$$F^+(\omega_n) = \frac{1}{AT}\int_{-T/2}^{T/2} dt_0 \int_{-T/2}^{T/2} dt' \times \theta(t'-t_0)\langle f(t')f(t_0)\rangle\, e^{i\omega_n(t'-t_0)}. \tag{30}$$

Note that the integration in Eq. (30) over the line $t = t' - t_0 = 0$ contributes to the entire integration *with only half of its original value* because we have set $\theta(0) = 1/2$ for the sum rule for $F^{\pm}(\omega)$ to be satisfied as per Eq. (27). Consequently, Eq. (24) is confirmed to safely hold, including the case of Eq. (25).

Taking this into account, we now use the discretized form of the unit step function:

$$\theta_k \equiv \left\{ \begin{array}{ll} 1 - \delta_{k,0}/2, & k \geqslant 0 \\ 0, & \text{otherwise} \end{array} \right\}, \tag{31}$$

where $\delta_{k,0}$ is the Kronecker δ and k is an integer. Using θ_k, Eq. (30) is discretized as

$$\begin{aligned} F^+(\omega_n) &= \frac{1}{A}\frac{1}{M\Delta t}\sum_{l=-M/2+1}^{M/2}\;\sum_{m=-M/2+1}^{M/2}(\Delta t)^2 \\ &\quad\times \theta_{m-l}\,\langle f(t_m)f(t_l)\rangle\, e^{i\omega_n(t_m-t_l)} \\ &= \frac{\Delta t}{AM}\sum_{l=-M/2+1}^{M/2}\;\sum_{m=l}^{M/2}\langle f(t_m)f(t_l)\rangle\, e^{i\omega_n(t_m-t_l)} \\ &\quad- \frac{\Delta t}{2AM}\sum_{l=-M/2+1}^{M/2}\langle f(t_l)f(t_l)\rangle. \end{aligned} \tag{32}$$

For computational convenience, we switch the order of the double summation in the first term, which gives *the discretized WKT-FLT equation for the relaxation function*:

$$\begin{aligned} F^+(\omega_n) &= \frac{\Delta t}{AM}\left\langle \sum_{m=-M/2+1}^{M/2} f(t_m)\, e^{i\omega_n t_m} \sum_{l=-M/2+1}^{m} f(t_l)\, e^{-i\omega_n t_l} \right\rangle \\ &\quad- \frac{\Delta t}{2}, \end{aligned} \tag{33}$$

where the variables and constants are the same as for Eq. (8). The second term is the correction term to eliminate the overcounting along the line $m = l$, which corresponds to the line $t = 0$ in the continuous case. The discretized function $F^-(\omega_n)$ is derived in the same way. The sum rules for the discretized WKT-FLT equations for $F^{\pm}(\omega_n)$ are easily confirmed by multiplying both sides of Eq. (33) by $\Delta\omega$ and summing from $n = -M/2 + 1$ to $M/2$ using the following representation of the Kronecker δ:

$$\delta_{m,l} = \frac{1}{M}\sum_{n=-M/2+1}^{M/2} e^{i\omega_n(t_m-t_l)}. \tag{34}$$

The relations involving $F(\omega_n)$, $F^+(\omega_n)$, and $F^-(\omega_n)$ hold in the same way as the relations for the continuous case [Eqs. (23)–(25)].

The discretized WKT-FLT equation can also be introduced into the simulation loop as done with the discretized WKT equation (see Appendix A). The only difference with the case

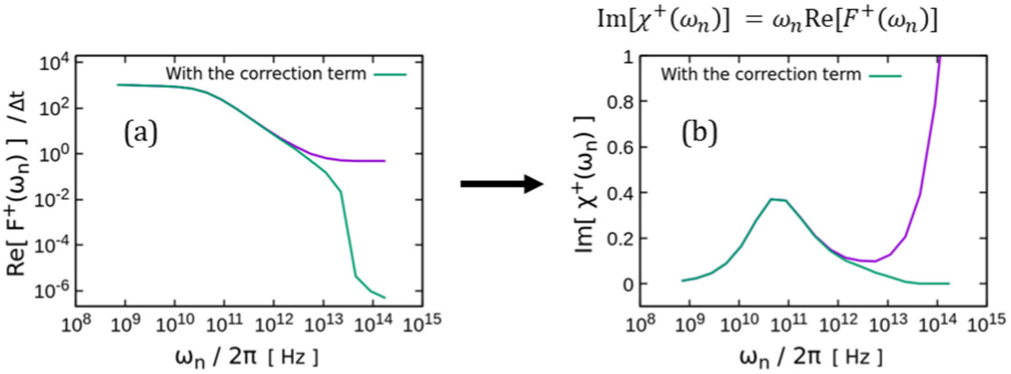

FIG. 3. Effects of the correction term in relaxation and response functions: (a) the real part of $F^+(\omega_n)$ and (b) the imaginary part of $\chi^+(\omega_n)$ for the bisect vectors $\mathbf{u}_j^{\vdash}(t)$ [illustrated in Fig. 1(a)] of the united atom polyethylene model at 500 K, obtained by MD simulation. The green and violet curves are computed by using the discretized WKT-FLT Eq. (33), with and without the correction term, respectively. The function $\chi^+(\omega_n)$ is converted from $F^+(\omega_n)$ by using Eq. (10). The artifacts observed in the violet curves are not present in the green curves.

for the WKT is the green-colored procedure in Fig. 9. The discretized WKT-FLT Eq. (33) is separated as follows:

$$F^+(\omega_n) = \frac{\Delta t}{AM}\langle g(\omega_n)\rangle - \frac{\Delta t}{2}, \tag{35}$$

$$g(\omega_n) = \sum_{m=-M/2+1}^{M/2} h(t_m, \omega_n), \tag{36}$$

and

$$h(t_m, \omega_n) = f(t_m)\, e^{i\omega_n t_m} \sum_{l=-M/2+1}^{m} f(t_l)\, e^{-i\omega_n t_l}. \tag{37}$$

In Eq. (35), to compute $F^+(\omega_n)$, we replace the statistical average $\langle\cdots\rangle$ with the average over the number of the simulations.

Using Eq. (A1), we thin out the unnecessary values of $F^+(\omega_n)$ and make space between the adjacent ω_n's. The value of $h(t_m, \omega_n)$ in Eq. (37) is computed every time step and is added to the array $g(\omega_n)$ of Eq. (36) during the simulation. After the end of the multiple simulations, substituting the computed $g(\omega_n)$ into Eq. (35) and taking the average over the number of simulations, we get $F^+(\omega_n)$ without storing the entire time series of $f(t_m)$ and without any lack of $f(t_m)$ during the simulations. We call this approach *the on-the-fly algorithm for the WKT-FLT*.

Figure 3 shows effects of the correction term in relaxation and response functions: (a) the real part of $F^+(\omega_n)$, (b) the imaginary part of $\chi^+(\omega_n)$, for the bisect vectors $\mathbf{u}_j^{\vdash}(t)$ [see Fig. 1(a)]. The function $F^+(\omega_n)$ is computed by using the discretized WKT-FLT Eq. (33), and $\chi^+(\omega_n)$ is converted from $F^+(\omega_n)$ by using Eq. (10). Figure 3 presents both results computed with and without the correction term. Due to the correction term, the artifact is removed from $\mathrm{Re}[F^+(\omega_n)]/\Delta t$ [Fig. 3(a)]: with the correction term, this quantity continues to decay with increasing ω_n (see green curve), whereas, without the correction term, it converges to 1/2 (see violet curve). As a result, the strange increase in $\mathrm{Im}[\chi^+(\omega_n)]$ for large ω_n is not present [Fig. 3(b)].

The source of the artifact in $\mathrm{Re}[F^+(\omega_n)]$ becomes clear; namely, it is due to the overcounting along the line $t = 0$ upon discretizing the WTK-FLT equation. Conversely, the source of the artifact in $\mathrm{Im}[F^+(\omega_n)]$ [Fig. 1(b)] remains unknown.

V. SOURCE OF ARTIFACT IN Im[$F^+(\omega_n)$]

As explained in the introduction, the real part of $\chi^+(\omega_n)$, converted from the imaginary part $F^+(\omega_n)$ by using Eq. (10) as $\mathrm{Re}[\chi^+(\omega_n)] = 1 - \omega_n \,\mathrm{Im}[F^+(\omega_n)]$, is expected to converge to zero with increasing ω_n. Thus, $\mathrm{Im}[F^+(\omega_n)]$ should asymptotically approach $1/\omega_n$ with increasing ω_n. Although $\mathrm{Im}[F^+(\omega_n)]$ in Fig. 1(b) appears to decrease proportionally to $1/\omega_n$ up to approximately 10^{13} Hz, it deviates from $1/\omega_n$ around 10^{14} Hz and drops to zero at $\omega_n = \pi/\Delta t$, where the $\pi/\Delta t$ is the maximum value of ω_n (called the Nyquist frequency).

We investigate this undesirable behavior of $\mathrm{Im}[F^+(\omega_n)]$ starting at Eq. (33). The equation for $\mathrm{Im}[F^+(\omega_n)]$ contains a factor of $\sin[\omega_n(t_m - t_l)]$ inside the double summation over l and m. The value of $\sin[\omega_n(t_m - t_l)]$ is zero at the Nyquist frequency $\omega_n = \pi/\Delta t$, because $t_m - t_l = \Delta t(m - l)$ from Eq. (8). We expand it up to first order in a Taylor series in the vicinity of $\omega_n = \pi/\Delta t$. The resulting first-order term contains the factor $(\omega_n - \pi/\Delta t)$ outside the summation:

$$\begin{aligned}\mathrm{Im}[F^+(\omega_n)] &= \frac{\Delta t}{AM}\sum_{m=-M/2+1}^{M/2}\sum_{l=-M/2+1}^{m}\langle f(t_m)f(t_l)\rangle \\ &\quad\times \sin\left[\omega_n(t_m - t_l)\right] \\ &\cong \frac{\Delta t}{AM}\left(\omega_n - \frac{\pi}{\Delta t}\right)\sum_{m=-M/2+1}^{M/2}\sum_{l=-M/2+1}^{m}\langle f(t_m)f(t_l)\rangle \\ &\quad\times (t_m - t_l)(-1)^{m-l} \\ &= \frac{\Delta t}{A}\left(\omega_n - \frac{\pi}{\Delta t}\right)\sum_{k=0}^{M/2}\langle f(t_k)f(0)\rangle t_k(-1)^k,\end{aligned} \tag{38}$$

where the double summation is changed to the single summation by using $\langle f(t_m)f(t_l)\rangle = \langle f(t_m - t_l)f(0)\rangle = \sum_{k=-M/2+1}^{M/2}\delta_{k,m-l}\langle f(t_k)f(0)\rangle$ and the discretized unit step function θ_k [Eq. (31)]. Although it is difficult to know the precise value of the summation after the expansion, we consider, based on the simulation results shown in Fig. 1(b) and the model calculation using the Debye relaxation model (see Appendix D), that it converges to a finite negative value. Thus, $\mathrm{Im}[F^+(\omega_n)]$ approaches $\omega_n = \pi/\Delta t$ proportionally to $-(\omega_n - \pi/\Delta t)$, and goes to zero at $\omega_n = \pi/\Delta t$. Accordingly, $\mathrm{Re}[\chi^+(\omega_n)] = 1 - \omega_n \mathrm{Im}[F^+(\omega_n)]$ increases with increasing ω_n around $\omega_n/2\pi = 10^{14}$ Hz and goes to unity at $\omega_n = \pi/\Delta t$, as in Fig. 1(d).

The Nyquist frequency $\omega_n = \pi/\Delta t$ does not appear in the finite-continuous Fourier transformation because the maximum value of ω_n (or n) can be set to $\pm\infty$. The Nyquist frequency only appears in the finite-discrete case. The finite-discrete $\mathrm{Im}[F^+(\omega_n)]$ is always zero at $\omega_n = \pi/\Delta t$, and there is no way for $\mathrm{Im}[F^+(\omega_n)]$ to approach $\omega_n = \pi/\Delta t$ except for $\mathrm{Im}[F^+(\omega_n)] \propto -(\omega_n - \pi/\Delta t)$ near $\omega_n = \pi/\Delta t$. Therefore, the source of the undesirable behavior of $\mathrm{Im}[F^+(\omega_n)]$ is the cutoff of the finite-discrete Fourier-Laplace transformation at the Nyquist frequency $\omega_n = \pi/\Delta t$. The source of the artifact in $\mathrm{Im}[F^+(\omega_n)]$ clearly differs from that in $\mathrm{Re}[F^+(\omega_n)]$ [see Sec. IV], although both artifacts are associated with the discretization of the WKT-FLT equation.

The Riemann-Lebesgue lemma states that the Fourier integral of an absolutely integrable function should converge to zero when ω or $\omega_n \to \infty$, whether the interval of the Fourier integral is finite or infinite [17]. It means that $F^+(\omega_n)$ and $\chi^+(\omega_n)$ analytically obtained by the finite-continuous Fourier-Laplace transformation converge to zero when $\omega_n \to \infty$, because $F(t)$ and $\chi(t)$ are absolutely integrable. Hence, both the $F^+(\omega_n)$ and $\chi^+(\omega_n)$ computed from the finite-discrete molecular simulations should also converge to zero at large ω_n. Actually, in Fig. 1(b), $\mathrm{Im}[F^+(\omega_n)]$ partially reproduces the features of $\approx 1/\omega_n$. Moreover, when plotting $\mathrm{Im}[F^+(\omega_n)]$ on the vertical axis instead of the logarithm of $\mathrm{Im}[F^+(\omega_n)]$ [as in Fig. 1(b)], $\mathrm{Im}[F^+(\omega_n)]$ appears to converge to zero. However, for the conversion of Eq. (10) not to produce the strange increase in $\mathrm{Re}[\chi^+(\omega_n)]$, $\mathrm{Im}[F^+(\omega_n)]$ must asymptotically approach $1/\omega_n$ but must not go to zero at $\omega_n = \pi/\Delta t$.

From the discussion here, it follows that the artifact observed in $\mathrm{Im}[F^+(\omega_n)]$ is caused by the cutoff at the Nyquist frequency $\omega_n = \pi/\Delta t$. The way in which $\mathrm{Im}[F^+(\omega_n)]$ approaches $\omega_n = \pi/\Delta t$ is different from the ideal case of $\approx 1/\omega_n$, which results in the strange increase of $\mathrm{Re}[\chi^+(\omega_n)]$ near $\omega_n = \pi/\Delta t$ through the conversion $\mathrm{Re}[\chi^+(\omega_n)] = 1 - \omega_n \mathrm{Im}[F^+(\omega_n)]$ [Eq. (10)]. Although the reason is simple, it is difficult to eliminate the source from $\mathrm{Im}[F^+(\omega_n)]$ and to remove the resulting artifact in $\mathrm{Re}[\chi^+(\omega_n)]$.

Incidentally, $\chi^+(\omega)$ can be written as the Fourier-Laplace transform of a time-domain response function $\chi(t)$ instead of the conversion from $F^+(\omega)$ via Eq. (10). In this case, the discretized equation for $\mathrm{Re}[\chi^+(\omega_n)]$ contains a correction term, same as that for $\mathrm{Re}[F^+(\omega_n)]$ in Eq. (33). The correction term should eliminate the overcounting, allowing $\mathrm{Re}[\chi^+(\omega_n)]$ to converge to zero for large ω_n. In addition, the discretized equation for $\mathrm{Im}[\chi^+(\omega_n)]$ contains the factor of $\sin[\omega_n(t_m - t_l)]$ inside the double summation, same as that for $\mathrm{Im}[F^+(\omega_n)]$ in Eq. (38). Similarly to $\mathrm{Im}[F^+(\omega_n)]$, $\mathrm{Im}[\chi^+(\omega_n)]$ should appear to converge to zero at large ω_n as long as plotting the linearly separated $\mathrm{Im}[\chi^+(\omega_n)]$ on the vertical axis, even though the asymptotic approach to the Nyquist frequency $\omega_n = \pi/\Delta t$ is not the ideal convergence. To remove the artifact, we must derive the discretized WKT-FLT equation designated for $\chi^+(\omega_n)$.

VI. DISCRETIZED WKT-FLT EQUATION FOR RESPONSE FUNCTION

This section derives the WKT-FLT equation for the response function $\chi^+(\omega)$ and then discretizes it.

The relation between the ACF $F(t)$ and the time-domain response function $\chi(t)$ is [9]

$$F(t) = \int_t^\infty \chi(s)\,ds = \int_{-\infty}^\infty \theta(s-t)\,\chi(s)\,ds, \tag{39}$$

where $\theta(s-t)$ is the Heaviside unit step function [Eq. (18)]. Differentiating Eq. (39) with respect to t gives

$$\chi(t) = -\frac{dF(t)}{dt}, \tag{40}$$

where $d\theta(t)/dt = \delta(t)$ is used. Substituting the ACF of Eq. (11) into the above equation gives

$$\begin{aligned}\chi(t) &= -\frac{1}{A}\langle \dot{f}(t+t_0) f(t_0)\rangle_{t_0} \\ &= -\frac{1}{A}\lim_{T\to\infty}\frac{1}{T}\int_{-T/2}^{T/2} dt_0\, \dot{f}(t+t_0) f(t_0),\end{aligned} \tag{41}$$

where the dotted quantities ($\dot{}$) are time derivatives.

Following the strategy used to derive the effective ACF $F_\mathrm{e}(t)$, we obtain an effective response function. We restrict the domain of $\dot{f}(t+t_0)$ to $-T/2 < t + t_0 < T/2$ as follows:

$$\begin{aligned}\dot{f}(t+t_0) &= \int_{-T/2}^{T/2} dt' f(t')\,\frac{d}{dt}\delta(t' - (t+t_0)) \\ &= \int_{-T/2}^{T/2} dt' \dot{f}(t')\,\delta(t' - (t+t_0)).\end{aligned} \tag{42}$$

Substituting Eq. (42) into Eq. (41), we get *the effective response function* $\chi_\mathrm{e}(t)$:

$$\begin{aligned}\chi(t) &\cong \chi_\mathrm{e}(t) \\ &= -\frac{1}{A}\lim_{T\to\infty}\frac{1}{T}\int_{-T/2}^{T/2} dt_0 \\ &\quad \times \int_{-T/2}^{T/2} dt' \dot{f}(t') f(t_0)\,\delta(t' - (t+t_0)).\end{aligned} \tag{43}$$

The frequency-domain response function $\chi^+(\omega)$ is obtained by the Fourier-Laplace transformation for $\chi(t)$:

$$\chi^+(\omega) = \int_0^\infty \chi(t)\,e^{i\omega t}\,dt = \int_{-\infty}^\infty \theta(t)\,\chi(t)\,e^{i\omega t}\,dt. \tag{44}$$

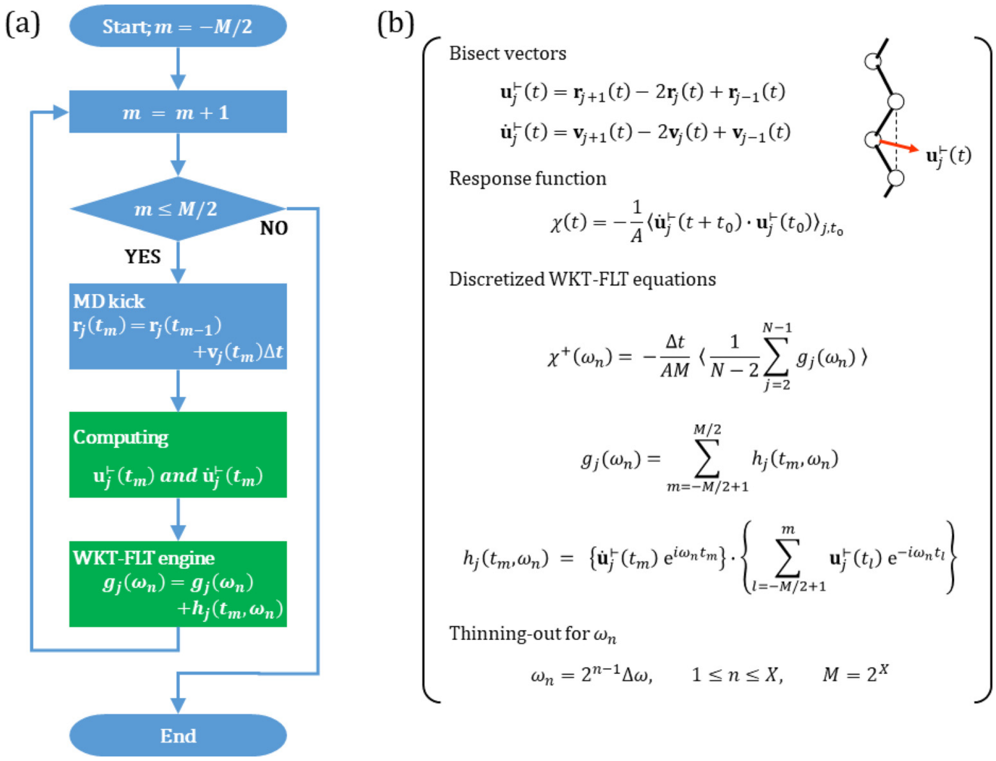

FIG. 4. On-the-fly algorithm for the WKT-FLT: (a) a flow chart of time loop of MD simulation and (b) equations for computing the frequency-domain response function $\chi^+(\omega_n)$ regarding the bisect vectors $\mathbf{u}_j^{\vdash}(t)$. Bisect vectors $\mathbf{u}_j^{\vdash}(t)$ and its time derivative $\dot{\mathbf{u}}_j^{\vdash}(t)$ are defined in the first and second equations in panel (b), where $\mathbf{r}_j(t)$ and $\mathbf{v}_j(t)$ are the position and velocity vectors of atom j, respectively. The time-domain response function $\chi(t)$, the discretized WKT-FLT equations for $\chi^+(\omega_n)$, and the equations for thinning out ω_n are also shown in panel (b). In panel (a), $\mathbf{u}_j^{\vdash}(t_m)$ and $\dot{\mathbf{u}}_j^{\vdash}(t_m)$ are computed by the first green-colored procedure. In the second green-colored procedure called WKT-FLT engine, $h_j(t_m, \omega_n)$ is computed at each time step and is added sequentially to the array of $g_j(\omega_n)$. After the end of the multiple simulations, substituting $g_j(\omega_n)$ into the first of the WKT-FLT equations and averaging over the number of simulations gives $\chi^+(\omega_n)$.

Substituting $\chi_e(t)$ [Eq. (43)] into Eq. (44) instead of $\chi(t)$ [Eq. (41)] gives *the WKT-FLT equation for the response function*:

$$\chi^+(\omega) = \int_0^\infty \chi_e(t)\, e^{i\omega t}\, dt$$
$$= -\frac{1}{A}\lim_{T\to\infty}\frac{1}{T}\int_{-T/2}^{T/2} dt_0\, f(t_0)\, e^{-i\omega t_0}$$
$$\times \int_{t_0}^{T/2} dt'\, \dot{f}(t')\, e^{i\omega t'}. \qquad (45)$$

Next, we discretize Eq. (45) by replacing the continuous ω with the discrete $\omega_n = 2\pi n/T$ and removing the limit on T from Eq. (45) by taking the statistical average $\langle\cdots\rangle$. We write it by using the unit step function $\theta(t)$:

$$\chi^+(\omega_n) = -\frac{1}{AT}\int_{-T/2}^{T/2} dt_0 \int_{-T/2}^{T/2} dt'$$
$$\times\, \theta(t'-t_0)\langle \dot{f}(t') f(t_0)\rangle\, e^{i\omega_n(t'-t_0)}. \qquad (46)$$

The integrals of Eq. (46) are discretized by using the discretized unit step function of Eq. (31):

$$\chi^+(\omega_n) = -\frac{1}{A}\frac{1}{M\Delta t}\sum_{l=-M/2+1}^{M/2}\sum_{m=-M/2+1}^{M/2}(\Delta t)^2$$
$$\times\, \theta_{m-l}\,\langle \dot{f}(t_m) f(t_l)\rangle\, e^{i\omega_n(t_m-t_l)}$$
$$= -\frac{\Delta t}{AM}\sum_{l=-M/2+1}^{M/2}\sum_{m=l}^{M/2}\langle \dot{f}(t_m) f(t_l)\rangle\, e^{i\omega_n(t_m-t_l)}$$
$$+ \frac{\Delta t}{2AM}\sum_{l=-M/2+1}^{M/2}\langle \dot{f}(t_l) f(t_l)\rangle. \qquad (47)$$

In Eq. (47), notice that the second term is zero because, at a given time t_l, a physical quantity $f(t_l)$ and its time derivative $\dot{f}(t_l)$ are uncorrelated [i.e., $\langle \dot{f}(t_l) f(t_l)\rangle = 0$] [9,21].

The final form of *the discretized WKT-FLT equation for the response function* is

$$\chi^+(\omega_n) = -\frac{\Delta t}{AM}\left\langle \sum_{m=-M/2+1}^{M/2} \dot{f}(t_m)\, e^{i\omega_n t_m}\sum_{l=-M/2+1}^{m} f(t_l)\, e^{-i\omega_n t_l}\right\rangle. \qquad (48)$$

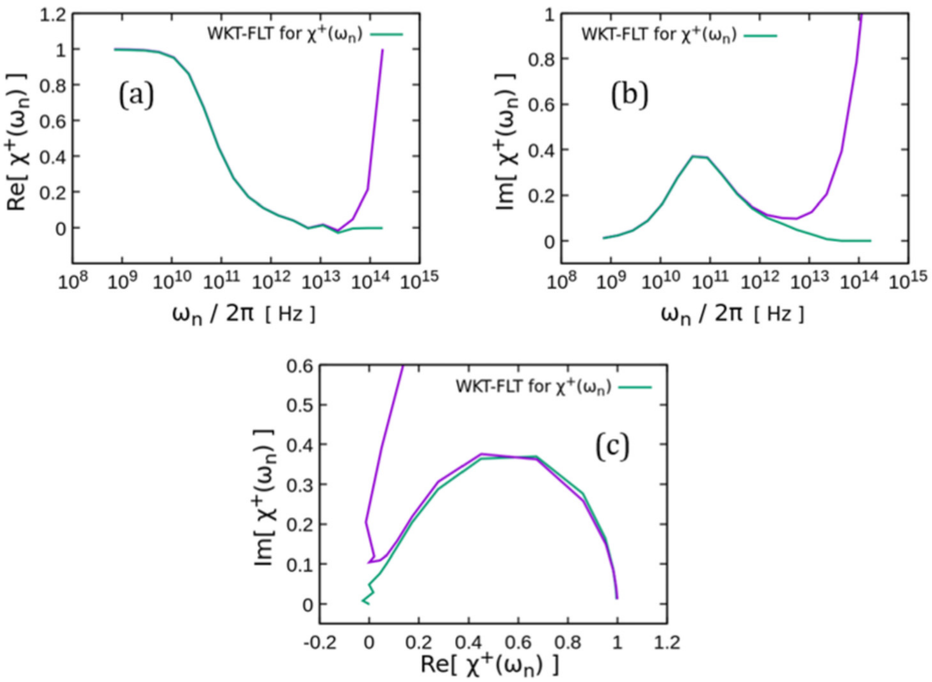

FIG. 5. Response function $\chi^+(\omega_n)$ for bisect vectors $\mathbf{u}_j^{\vdash}(t)$ of a united atom polyethylene model at 500 K, obtained by MD simulation using the on-the-fly algorithm of Fig. 4. Panels (a) and (b) plot the real part and imaginary part of $\chi^+(\omega_n)$ versus $\log \omega_n$, respectively. Panel (c) is a Cole-Cole plot of the real and imaginary parts. The violet curves are obtained from the conversion from $F^+(\omega_n)$ (without the correction term) using Eq. (10). The green curves are obtained from the designated WKT-FLT for the response function $\chi^+(\omega_n)$ [Eq. (48)]. In panels (a) and (b), the strange increases at large ω_n in the violet curves are not present in the green curves. Also, in panel (c), the error observed on the left side of the half circle in the violet curve disappears in the green curve.

Contrary to our expectation in Sec. V, Eq. (48) does not have the correction term. Although the correction term to eliminate the overcounting along the line $m = l$ emerges in Eq. (47), it disappears due to the noncorrelation between a physical quantity and its time derivative at a given time.

The discretized WKT-FLT equation for $\chi^+(\omega_n)$ can also be introduced into the simulation loop as done with $F^+(\omega_n)$. We separate the discretized WKT-FLT Eq. (48) as follows:

$$\chi^+(\omega_n) = -\frac{\Delta t}{AM}\langle g(\omega_n)\rangle, \tag{49}$$

$$g(\omega_n) = \sum_{m=-M/2+1}^{M/2} h(t_m, \omega_n), \tag{50}$$

and

$$h(t_m, \omega_n) = \dot{f}(t_m)\, e^{i\omega_n t_m} \sum_{l=-M/2+1}^{m} f(t_l)\, e^{-i\omega_n t_l}. \tag{51}$$

Using Eq. (A1), we can thin out unnecessary values of $\chi^+(\omega_n)$. During the simulation, the function $h(t_m, \omega_n)$ of Eq. (51) is computed every time step m and is added to the array $g(\omega_n)$ of Eq. (50). After the multiple simulations, we get $\chi^+(\omega_n)$ by substituting the computed $g(\omega_n)$ into Eq. (49) and taking the average over the number of the simulations. Figure 4 shows an outline of the on-the-fly algorithm for the WKT-FLT for a response function $\chi^+(\omega_n)$, which describes as an example the computation of the $\chi^+(\omega_n)$ for the bisect vectors $\mathbf{u}_j^{\vdash}(t)$ of a polymer chain.

Figure 5 shows the response function $\chi^+(\omega_n)$ for bisect vectors $\mathbf{u}_j^{\vdash}(t)$, computed for a united atom polyethylene model at 500 K. Figures 5(a) and 5(b) plot the real and imaginary parts of $\chi^+(\omega_n)$ computed by Eq. (48) (green curves) as functions of $\log \omega_n$. In addition, $\chi^+(\omega_n)$ converted from $F^+(\omega_n)$ (without the correction term) by using Eq. (10) is also plotted (violet curves). The strange increases in both the real and imaginary parts of the violet curves at high ω_n are not present in the green curves. Figure 5(c) shows a Cole-Cole plot [9,22,23] for $\chi^+(\omega_n)$; the error on the left side of the half circle in the violet curve disappears in the green curve. Thus, the artifacts in both the real and imaginary parts of $\chi^+(\omega_n)$ are removed upon using the discretized WKT-FLT equation designated for $\chi^+(\omega_n)$.

VII. APPLICATION EXAMPLES

Figure 9 in Appendix A presents an example of the computation of the frequency-domain velocity correlation function and Fig. 4 shows the computation of the frequency-domain response function of the bisect vectors. In this section, we show the other examples of the spectroscopic analysis using the WKT-FLT equations with the artifacts removed.

A. Wave-vector-dependent dynamic susceptibility in an isotropic amorphous state of polyethylene

Isotropic amorphous state is one of the fundamental states when considering the materials science. In this subsection, we show the computed results of “wave-vector-dependent

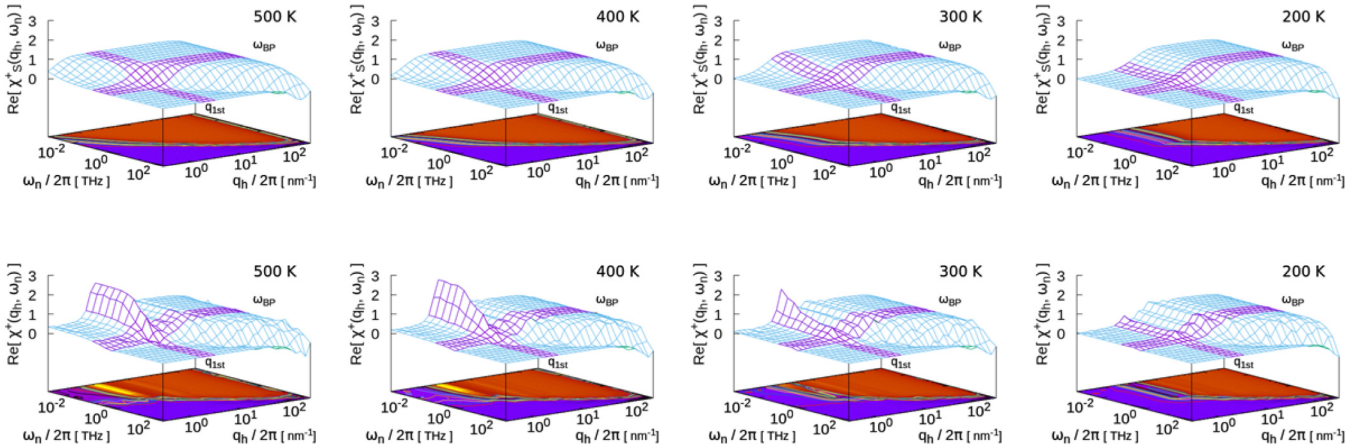

FIG. 6. Three-dimensional graphs of the real part of $\chi_{\mathrm{s}}^{+}(q_h, \omega_n)$ (upper row) and $\chi^{+}(q_h, \omega_n)$ (lower row) computed for the model polyethylene system and plotted against the logarithm of q_h and ω_n. From left to right are shown the profiles for 500, 400, 300, and 200 K. The violet belts indicate the first peak position of the static structure factor $S(q_h)$ ($q_{1\mathrm{st}}$) and the position of the low-energy excitation in Fig. 9(c) (ω_{BP}).

dynamic susceptibility" [9,19] for an isotropic amorphous polyethylene system.

Starting from the van Hove time-space density correlation function for classical systems [24], we derive the discretized WKT-FLT equations of the wave-vector-dependent dynamic susceptibilities of the coherent (full-correlation) part $\chi^{+}(\mathbf{q_h}, \omega_n)$ and the incoherent (self-correlation) part $\chi_{\mathrm{s}}^{+}(\mathbf{q_h}, \omega_n)$ (see Appendix E for the derivations), where $\mathbf{q_h}$ is a discrete wave vector. To obtain $\chi^{+}(\mathbf{q_h}, \omega_n)$ and $\chi_{\mathrm{s}}^{+}(\mathbf{q_h}, \omega_n)$ in a wide temperature range, cooling MD simulations of the united atom polyethylene model are performed from 800 K to 12.5 K under 1 atm. Then, we implement NVE constant simulations using the states on the way of the cooling as initial states. During the NVE simulations, $\chi^{+}(\mathbf{q_h}, \omega_n)$ and $\chi_{\mathrm{s}}^{+}(\mathbf{q_h}, \omega_n)$ are computed with the on-the-fly algorithm for the WKT-FLT (see Appendix F 1 for the simulation outline).

Figure 6 plots the real parts of $\chi_{\mathrm{s}}^{+}(q_h, \omega_n)$ (upper row) and $\chi^{+}(q_h, \omega_n)$ (lower row) as a function of the logarithm of q_h and ω_n. Because it takes a long time to compute $\chi^{+}(\mathbf{q_h}, \omega_n)$ and $\chi_{\mathrm{s}}^{+}(\mathbf{q_h}, \omega_n)$ for all wave vector $\mathbf{q_h}$, we only compute the mean value of the following components of $\chi^{+}(\mathbf{q_h}, \omega_n)$ and $\chi_{\mathrm{s}}^{+}(\mathbf{q_h}, \omega_n)$:

$$\begin{aligned}\chi^{+}(q_h, \omega_n) = {} & \tfrac{1}{3}\{\chi^{+}((q_h, 0, 0), \omega_n) \\ & + \chi^{+}((0, q_h, 0), \omega_n) + \chi^{+}((0, 0, q_h), \omega_n)\}, \\ & q_h = h\Delta q, h = 1, 2, 3, \ldots. \end{aligned} \tag{52}$$

In the upper row of Fig. 6, the three-dimensional (3D) graphs change gradually with decreasing temperature. At 500 K, a single step appears connecting the low-q_h and -ω_n region diagonally to the high-q_h and -ω_n region. With decreasing temperature, the part of the step located around the low-ω_n range shifts to the high-q_h range. At 200 K, the step in the low-ω_n range becomes parallel to the ω_n axis, whereas the step in the high-q_h and -ω_n range remains diagonal, and the two steps intersect around $\omega_n/2\pi = 3.0 \times 10^{11}$ Hz ($\equiv \omega_{\mathrm{BP}}/2\pi$), which corresponds to the frequency of the low-energy excitation

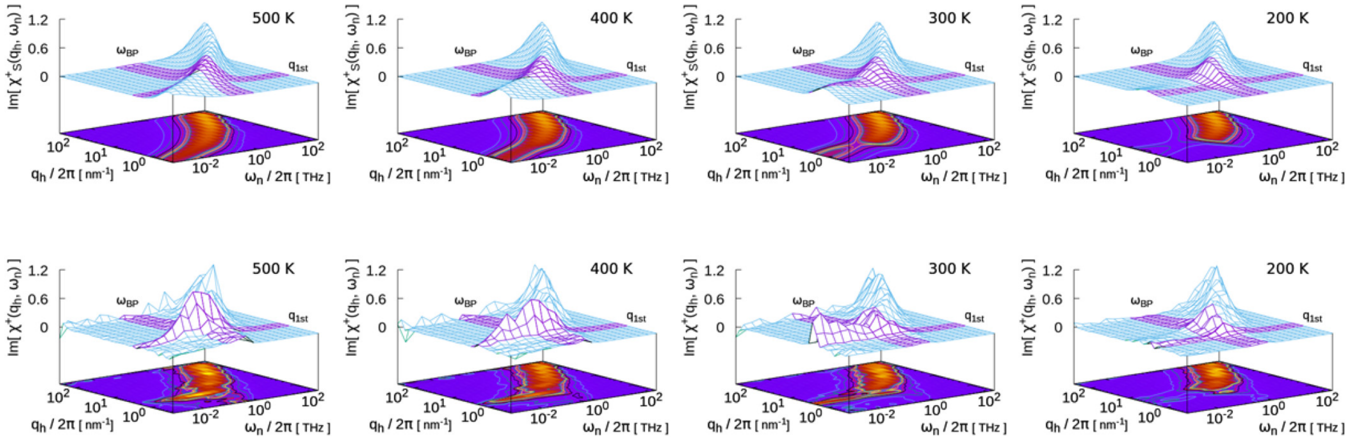

FIG. 7. Three-dimensional graphs of the imaginary part of $\chi_{\mathrm{s}}^{+}(q_h, \omega_n)$ (upper row) and $\chi^{+}(q_h, \omega_n)$ (lower row) computed in the model polyethylene system are plotted against logarithm of q_h and ω_n. From the left side to right side, the data of 500, 400, 300, and 200 K are aligned. The violet belts indicate the first peak positon of $S(q_h)$ ($q_{1\mathrm{st}}$) and the position of the low-energy excitation in Fig. 9(c) (ω_{BP}), respectively. Comparing with Fig. 6, the graphs are rotated around the vertical axes by 90° counterclockwise.

shown in Fig. 9(c). The low-energy excitation is considered to originate from the excess vibrational states (called "Boson peak") observed in the vibrational density of states of low-temperature glasses [25–34]. Conversely, in the lower row, the 3D graphs are noisier than in the upper row, where the lower graphs look like that the upper graphs are multiplied by the static structure factor $S(q_h)$ [35] (see Fig. 15 in Appendix F 1). At the high temperatures, a strong streak appears on the line $q_h/2\pi = 2.0 \times 10^9\ \mathrm{m}^{-1}$ ($\equiv q_{1\mathrm{st}}/2\pi$) in the low-$\omega_n$ region. This line corresponds to the first peak position of the $S(q_h)$. The streak shifts to the low-ω_n with decreasing temperature and goes out from the window at 200 K.

Figure 7 plots the results for the imaginary parts of $\chi_s^+(q_h, \omega_n)$ (upper row) and $\chi^+(q_h, \omega_n)$ (lower row). In the upper row, a single ridge extends diagonally from the low-q_h and -ω_n region to the high-q_h and -ω_n region. As the temperature decreases, the ridge located around the low-ω_n range shifts toward the high-q_h range, as occurs for the real part in Fig. 6. The ridge in the low-ω_n region disappears at 200 K, where the remaining ridge terminates around $\omega_{\mathrm{BP}}/2\pi$. In the lower row of Fig. 7, a strong peak appears on the same line $q_h/2\pi = q_{1\mathrm{st}}/2\pi$ as for the strong streak in Fig. 6. As the temperature decreases, the peak shifts to the low-ω_n with changing its shape and is not present at 200 K.

At 200 K in the upper rows of Figs. 6 and 7, the point where the two steps intersect is the same where the ridge terminates; this point shifts toward the higher $q_h/2\pi$ on the line $\omega_n/2\pi = \omega_{\mathrm{BP}}/2\pi$ with further cooling. The $q_h/2\pi$ value of this point might link to the spatial scale of the low-energy excitation [30,31].

At the high temperatures in the lower rows of Figs. 6 and 7, the streak and peak on the line $q_h/2\pi = q_{1\mathrm{st}}/2\pi$ indicate the existence of the cooperative motion between the nearest neighbor atoms. Conversely, because there is almost no intensity on the same line at 200 K, we see that the atom's motions become uncorrelated even between the nearest neighbors; i.e., the localized motions are dominant at 200 K. The behavior of the strong streak and peak as a function of temperature should be connected to the glass transition around 200 K that occurs in the simulations based on polyethylene molecular models [32,35,36].

B. Molecular rotation in *n*-octane crystals

Normal-alkane crystals exhibit the first-order solid-solid phase transition [37–42]. The differences in the dynamical properties between those in the high- and low-temperature phases are interesting in terms of the materials application and the physics of phase transitions.

As a preparation for the future precise investigations, we reproduce the solid-solid phase transition of the united atom *n*-octane (C_8H_{18}) crystal by cooling MD simulations from 200 K to 6.25 K under 1 atm. Then, NVE constant simulations are performed using the states on the way of the cooling as initial states, where the frequency-domain response functions of several orientation vectors are computed with the on-the-fly algorithm for the WKT-FLT (see Appendix F 2 for the simulation outline). The discretized WKT-FLT equations are obtained by replacing the bisect vector with the target orientation vectors in the equations of Fig. 4(b).

Figure 8 presents the frequency-domain response functions of *n*-alkane orientation vectors in crystal: the schematic illustrations of the orientation vectors [Figs. 8(a) and 8(b)] and the computed results [Fig. 8(c)]. Here we consider three

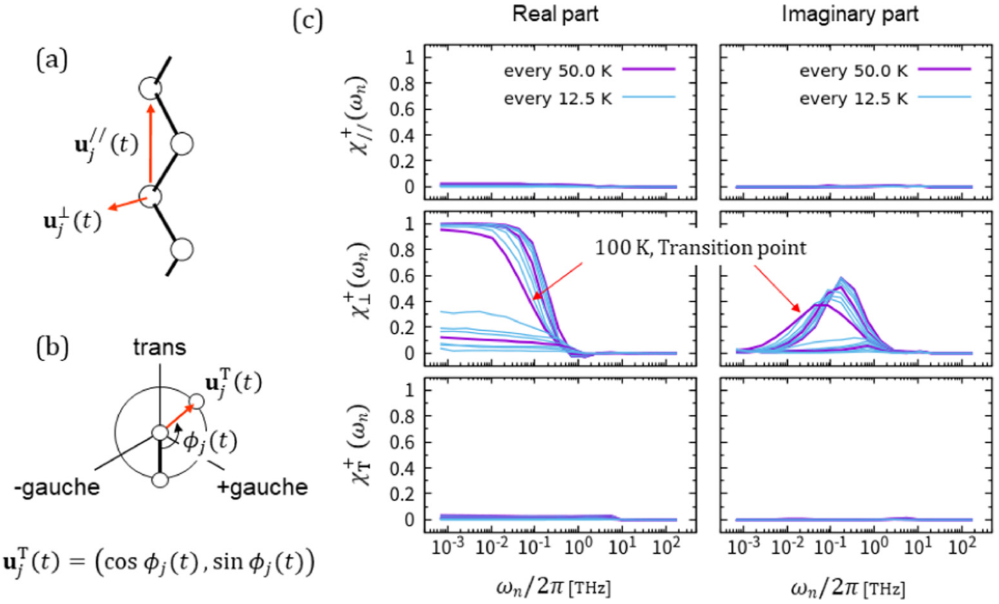

FIG. 8. Frequency-domain response functions of *n*-alkane orientation vectors in crystal. Panel (a) shows the schematic illustration of the parallel vector $\mathbf{u}_j^{//}(t)$ and the perpendicular vector $\mathbf{u}_j^{\perp}(t)$. Panel (b) is the torsion vector $\mathbf{u}_j^{\mathrm{T}}(t)$, where $\phi_j(t)$ is the dihedral angle. In panel (c), the result of the frequency-domain response functions $\chi_{//}(\omega_n)$ (parallel), $\chi_{\perp}(\omega_n)$ (perpendicular), and $\chi_{\mathrm{T}}(\omega_n)$ (torsion) are arranged from the top to the bottom; the left and right columns are the real and imaginary parts of them. In the middle row of the panel (c), two curves at 100 K are pointed by the red arrows, around which the solid-solid phase transition occurs from the high-temperature rotator phase to the low-temperature phase.

orientation vectors. In both high and low-temperature crystals, an *n*-alkane molecule has a strong tendency to take a planar-zigzag structure, in which each dihedral angle takes energetically the most stable conformation called ‘trans’ conformation [Fig. 8(b)]. As a result, the molecule stretches along an axis called the “molecular axis,” and the molecules align with pointing on average their molecular axes at the direction along the ‘*c* axis’ of the unit cell (see Fig. 16 in Appendix F 2). In such a crystal, the directions of the parallel vectors $\mathbf{u}_j^{//}(t)$ and the perpendicular vectors $\mathbf{u}_j^{\perp}(t)$ in a molecule [Fig. 8(a)] roughly correspond to the direction along the molecular axis and that perpendicular to the zigzag plane, respectively. Hence, we can investigate the swinging motion of the directions of the molecular axes and the rotating motion of the molecules around their molecular axes with the frequency-domain response functions for the parallel vector $\mathbf{u}_j^{//}(t)$ and the perpendicular vector $\mathbf{u}_j^{\perp}(t)$, respectively. Conversely, when two dihedral angles in a molecule take ‘+gauche’ and ‘−gauche’ conformations of the secondary stable conformations [Fig. 8(b)] with including at least more than one trans conformation between the +gauche and −gauche, the molecule takes a “kink” structure observed specifically in the high-temperature phase of the *n*-alkane crystal. We can see the dynamical feature of the kink structures with the frequency-domain response function for the torsion vector $\mathbf{u}_j^{\mathrm{T}}(t)$.

Panel (c) in Fig. 8 shows the frequency-domain response functions $\chi_{//}^{+}(\omega_n)$, $\chi_{\perp}^{+}(\omega_n)$ and $\chi_{\mathrm{T}}^{+}(\omega_n)$ for the parallel vector $\mathbf{u}_j^{//}(t)$, the perpendicular vector $\mathbf{u}_j^{\perp}(t)$ and the torsion vector $\mathbf{u}_j^{\mathrm{T}}(t)$, respectively. In the upper and lower rows, the curves are almost flat in the whole temperature range. In the middle row, at the high temperatures above 100 K, we observe the step- and bell-shaped curves in the real and imaginary parts, respectively. The step- and bell-shaped curves shift to the low-ω_n with decreasing temperature and collapse abruptly around 100 K, which is the phase transition point (see Fig. 16).

These results tell us that the *n*-octane molecules cannot swing the directions of the molecular axes largely and cannot make kinks in themselves frequently, throughout the simulations. Conversely, the molecules are actively rotating around the molecular axes in the high-temperature phase (the so-called “rotator phase” [43–47]). In the low-temperature phase, the rotation is prohibited because of the denser packing between the molecules, so that the step- and bell-shaped curves collapse below the transition point of 100 K.

From the peak position (≅60 GHz) of the imaginary part at 100 K, we see that the phase transition occurs when the relaxation time of the rotation becomes about 17 ps. It would be interesting to investigate the relation between the relaxation time and the transition temperature with changing the molecular length. Further investigation with the more realistic molecular models will contribute for understanding the *n*-alkane materials and their solid-solid phase transition from the viewpoint of the molecular rotation dynamics [37,38,46,47].

VIII. DISCUSSION

Textbooks on signal processing and analysis [3] discuss the overcounting along the line $\omega_n = 0$ together with the overcounting along the Nyquist-frequency line $|\omega_n| = \pi/\Delta t$ in the case of discrete inverse Fourier-Laplace transformations. The problem of overcounting is thus already recognized in the field of signal processing. However, Ref. [3] states that overcounting does not affect the computed results and can usually be ignored. In the present case, the artifact in $\mathrm{Re}[F^{+}(\omega_n)]$ is clearly connected to the overcounting along the line $t = 0$ and gives rise to the strange increase in $\mathrm{Im}[\chi^{+}(\omega_n)]$ in the high-frequency region as observed in Fig. 3. Therefore, in the present case, the overcounting produces a stronger effect than that in the case treated in Ref. [3]. Conversely, we do not consider the overcounting along the edge of the integration interval of $|t| = T/2$ because the correlation between two values $f(t+t_0)$ and $f(t_0)$ for $|t| = T/2$ should be very weak if T is sufficiently large.

Incidentally, note that $\mathrm{Im}[F^{+}(\omega_n)]$ computed by Eq. (33) retains the artifact caused by the cutoff [see Fig. 1(b)] simply because its source has not been eliminated; the approach of $\mathrm{Im}[F^{+}(\omega_n)]$ to the Nyquist frequency still differs from the ideal case of $\approx 1/\omega_n$. However, when we plot linearly separated $\mathrm{Im}[F^{+}(\omega_n)]$ on the vertical axis [instead of logarithmically separated as in Fig. 1(b)], $\mathrm{Im}[F^{+}(\omega_n)]$ appears to converge to zero at large ω_n. In Fig. 5(b), the same holds for $\mathrm{Im}[\chi^{+}(\omega_n)]$ (green curve) computed by Eq. (48). When we use the designated discretized WKT-FLT Eqs. (33) and (48) to compute $F^{+}(\omega_n)$ and $\chi^{+}(\omega_n)$, the artifacts in their imaginary parts do not matter provided (i) we are not interested in how the functions approach the Nyquist frequency and (ii) we plot the linearly separated $\mathrm{Im}[F^{+}(\omega_n)]$ and $\mathrm{Im}[\chi^{+}(\omega_n)]$ on the vertical axes.

Although we have not shown any results for the inverse conversion from $\chi^{+}(\omega_n)$ to $F^{+}(\omega_n)$ using $\chi^{+}(\omega) = 1 + i\omega F^{+}(\omega)$ [Eq. (10)], the function $F^{+}(\omega_n)$ converted from $\chi^{+}(\omega_n)$, which is computed by the designated equation for $\chi^{+}(\omega_n)$ [Eq. (48)], does not agree well at low or high ω_n with that computed by the designated equation for $F^{+}(\omega_n)$ [Eq. (33)]. We conclude that the discretized WKT-FLT Eqs. (33) and (48) are not compatible with Eq. (10). To obtain the frequency-domain functions, the designated WKT-FLT equations are preferable, and it is better to avoid the conversion between $\chi^{+}(\omega_n)$ and $F^{+}(\omega_n)$ via Eq. (10).

The time-domain functions expressed by the double integral with the Dirac δ function play important roles in this research. In Secs. II, III, and VI, one may directly obtain the WKT or WKT-FLT equations by the Fourier or Fourier-Laplace transformation for the effective ACF $F_{\mathrm{e}}(t)$ and the effective response function $\chi_{\mathrm{e}}(t)$, respectively. Usually, the derivations of the WKT or WKT-FLT equations require several mathematical steps; however, thanks to the effective functions $F_{\mathrm{e}}(t)$ and $\chi_{\mathrm{e}}(t)$, such calculations are not needed.

The WKT expresses the frequency-domain relaxation function $F(\omega)$ through the power spectral density $I(\omega)$; $F(\omega) = I(\omega)$. Conversely, the following relation expresses the time-domain relaxation function, ACF $F(t) = \langle f(t)f(0)\rangle/A$, through the effective ACF $F_{\mathrm{e}}(t)$:

$$\frac{1}{A}\langle f(t)f(0)\rangle \cong \frac{1}{A}\lim_{T\to\infty}\frac{1}{T}\int_{-T/2}^{T/2}dt_0\int_{-T/2}^{T/2}dt'f(t')f(t_0) \times \delta(t'-(t+t_0)). \tag{53}$$

The Fourier transform of Eq. (53) corresponds to the WKT Eq. (2), and the inverse Fourier transform of Eq. (2) corresponds to Eq. (53). In other words, Eq. (53) is *the time-domain WKT equation* as a counterpart of the frequency-domain WKT Eq. (2). Readers would already have noticed in Sec. II that the effective ACF $F_e(t)$ is the inverse Fourier transform of the power spectral density $I(\omega)$. Thus, Eq. (53) holds provided the WKT holds; the notation $\cong$ is thus valid when the requirements for the WKT are satisfied.

Statistical physics textbooks [9] state that, for the WKT Eq. (2) to hold, unnecessary terms should be omitted by taking the limit $T \to \infty$, where the convergences of the Fourier integrals of the ACF $F(t)$ and the function $tF(t)$ are required (see Appendix C for details). Of course, the requirements for the WKT are correct in the infinite-continuous case. However, we must consider how to obtain reliable spectroscopic data from the finite-discrete molecular simulations. The discretization for the Fourier-transform equations might give rise to unexpected errors, as we have seen in this research. Therefore, more concrete and specific requirements are needed for the discretized WKT. Omitting the unnecessary terms [9] links to ignoring the highlighted areas with the dashed lines on the plane of t' versus t_0 in Figs. 10(a) and 11(a) in Appendix B. We now investigate the requirements for the WKT in various cases using the ACFs expressed by the double integrals on the t' versus t_0 plane.

The time-domain WKT equation (53) can be applied to the Green-Kubo relation [6–8]. Integrating both sides of Eq. (53) over t with a single-side infinite integration interval gives

$$\begin{aligned}\frac{1}{A}\int_0^\infty dt\,\langle f(t)f(0)\rangle &= \frac{1}{2A}\int_{-\infty}^\infty dt\,\langle f(t)f(0)\rangle\\ &\cong \frac{1}{2A}\lim_{T\to\infty}\frac{1}{T}\int_{-T/2}^{T/2} dt_0\\ &\quad\times\int_{-T/2}^{T/2} dt' f(t')f(t_0)\\ &\quad\times\int_{-\infty}^{\infty} dt\,\delta(t'-(t+t_0))\\ &= \frac{1}{2A}\lim_{T\to\infty}\frac{1}{T}\left\{\int_{-T/2}^{T/2} dt\, f(t)\right\}^2. \end{aligned} \tag{54}$$

According to the Green-Kubo relation, the left-hand side of Eq. (54) gives the transport coefficient. The relation between the left-hand side and the right-hand side is discussed in the literature [8,48,49] and is used to obtain arbitrary transport coefficients from molecular simulations. The discretized equation for Eq. (54) corresponds to Eq. (6) with setting $\omega_n = 0$. Hence, by setting $\omega_n = 0$ in Fig. 9(b), we immediately obtain *the on-the-fly algorithm for the Green-Kubo relation*, where the mobility (or diffusion coefficient) can be computed. Again, the notation $\cong$ in Eq. (54) is valid when the usual requirements for the WKT are satisfied because we use the time-domain WKT in Eq. (54). However, the requirements for the discretized case are still unclear, which should also be known when using Eq. (54) to compute the transport coefficients from finite-discrete molecular simulations.

Although the time-domain WKT itself is not the subject of the present research, we confirm that both the frequency-domain WKT [Eq. (2)] and the Green-Kubo relation [Eq. (54)] can be derived by the Fourier integration over t and by the integration over t, for the time-domain WKT [Eq. (53)], respectively. The frequency-domain WKT and the Green-Kubo relation are connected through the time-domain WKT. It would thus be of interest to further investigate the time-domain WKT.

The on-the-fly algorithm, developed by Matsui and coworkers [18–20], can also be applied to obtain the frequency-domain relaxation and response functions for linearly separated ω_n instead of log-separated ω_n. Thus, the algorithm works for computing the high-frequency data comparable to the experimental spectra, such as infrared absorption or Raman scattering spectra [10–16,50–52]. The primary benefit of the on-the-fly algorithm is its simplicity; the postsimulation calculation is reduced dramatically by this algorithm even without the thinning out for ω_n. Conversely, the experimental spectra of low-frequency phenomena are usually complex spectra and are plotted versus log ω_n in most cases [23,53–55]. Thus, the discretized WKT-FLT equations show their true strength when applied to the low-frequency phenomena using the on-the-fly algorithm with ω_n thinned out. Consequently, the computation of the complex relaxation and response functions in a wide frequency range becomes significantly more efficient.

Ramírez and co-workers developed an algorithm for computing coarse-grained time-domain relaxation functions (they said "time-correlation functions") on the fly during simulations [56]. Their method is widely used to investigate various phenomena spanning a wide time range in the molecular simulations. We may also apply it to obtain the time-domain response functions. In this research, we have shown the way to compute the frequency-domain functions with the artifacts removed in a wide frequency range. As a result, we now have the methods to get the relaxation and response functions for wide ranges of both log t_m and log ω_n. We will be able to use these methods complementary to each other depending on the problems that we are interested in.

Although we show the examples of the MD simulations of the chain molecules in Sec. VII, the method presented herein can easily be combined with various simulation methods that reproduce other solid or liquid systems. Moreover, the discretized WKT-FLT should work well to see the invisible spectroscopic data, for example, the imaginary parts of the dynamic scattering functions or the spectra consisting of inactive degrees of freedom to external fields. We hope that the spectroscopic analysis using the discretized WKT-FLT with the on-the-fly algorithm for molecular simulations prove useful for investigating various molecular processes in material and biological applications.

IX. CONCLUSIONS

The two goals of this research are described in the introduction. The results of this research lead to the following conclusions:

(1) We investigated the sources of the artifacts observed in the numerical results computed by the WKT-FLT equation for

the frequency-domain relaxation function $F^+(\omega_n)$. The source of the artifact in $\mathrm{Re}[F^+(\omega_n)]$ is the overcounting along the line $t = 0$ when the WKT-FLT equation is discretized. In contrast, the source of the artifact in $\mathrm{Im}[F^+(\omega_n)]$ is the cutoff of the finite-discrete WKT-FLT equation at the Nyquist frequency. Through the conversion $\chi^+(\omega) = 1 + i\omega F^+(\omega)$, the artifacts yield similar strange increases in the real and imaginary parts of the frequency-domain response function $\chi^+(\omega_n)$ at high frequency. Although both of these sources are associated with the discretization of the WKT-FLT equation for $F^+(\omega_n)$, they differ from each other.

(2) Taking the sources of the artifacts into account, we derived a discretized WKT-FLT equation for $F^+(\omega_n)$ that included a correction term for the overcounting. Also, we derived the discretized WKT-FLT equation for $\chi^+(\omega_n)$. When using these corrected equations, the artifacts in $F^+(\omega_n)$ and $\chi^+(\omega_n)$ are removed.

(3) The equation for the conversion $\chi^+(\omega) = 1 + i\omega F^+(\omega)$ is not compatible with the discretized WKT-FLT equations. Therefore, we recommend avoiding the conversion and instead computing $F^+(\omega_n)$ and $\chi^+(\omega_n)$ by using the equations designated for this purpose [Eqs. (33) and (48)].

(4) We presented the on-the-fly algorithm for the WKT-FLT in the form of a flow chart. We also showed the computed results of the wave-vector-dependent dynamic susceptibilities in the isotropic amorphous polyethylene and the frequency-domain response functions of the orientation vectors in the *n*-alkane crystal, as examples of the spectroscopic analysis in molecular simulations.

More concrete and specific requirements for the WKT should become known when we apply it to molecular simulations. If successful, we should be able to use with confidence not only the WKT but also the WKT-FLT and the Green-Kubo relation for molecular simulations. Such research will be the subject of future presentations.

ACKNOWLEDGMENTS

This research was supported by funding from National Institute of Technology, Toyota College, Japan, for the overseas training program. We would like to express our gratitude to KIOXIA Co. for providing NVMe solid-state drives for this research. In addition, we would like to thank Prof. Takashi Odagaki and Dr. Jun Matsui for their helpful comments.

APPENDIX A: ON-THE-FLY ALGORITHM COMBINED WITH THE THINNING OUT FOR THE ANGULAR FREQUENCY

The on-the-fly algorithm combined with the thinning out of the angular frequency ω_n is essential for computing frequency-domain functions spanning a wide range of $\log \omega_n$. For clarity, we explain the algorithm by applying it to the discretized WKT [Eqs. (6)–(8)]. In Secs. IV, VI, and VII, we use this algorithm for implementing the WKT-FLT.

For high-frequency phenomena, a large simulation time steps M is not required. In this case, we can store the complete time series $f(t_m)$ in the computer's storage and can implement the WKT according to the procedures written in Sec. I. Conversely, for low-frequency phenomena (for which M is large), it becomes hard to output and store the value of $f(t_m)$ at every time step because the input-output time and total amount of the data become huge. In addition, it takes a long time to compute the Fourier transform $f(\omega_n)$ using Eq. (7) after the simulations. Moreover, it becomes harder when the time series contains the positions or velocities of the atoms in the system. How can we use the WKT for low-frequency phenomena? It is realized by thinning out the angular frequency ω_n combined with an on-the-fly algorithm [18–20] developed by Matsui and co-workers.

We usually compare the simulation results with experimental results. If the experimental results are spectroscopic data of low-frequency phenomena such as complex dielectric constants or dynamic viscoelastic moduli, $F(\omega_n)$ need not be computed for all angular frequencies because the experimental data are often plotted versus the logarithm of frequency. We can thus thin out the unnecessary values of $F(\omega_n)$ and make space between the adjacent ω_n's. For example, the expression for ω_n in Eq. (8) can be changed to

$$\omega_n = 2^{n-1}\Delta\omega, \quad 1 \leqslant n \leqslant X, \ M = 2^X. \tag{A1}$$

By doing this, the memory that should be allocated for the array of $f(\omega_n)$ can be drastically reduced and a large array for $f(\omega_n)$ need not be set aside. For example, even for $F(\omega_n)$ from a simulation of $M = 2^{30} (>10^9)$ steps, preparing an array of $f(\omega_n)$ with 30 components suffices by setting $X = 30$ in Eq. (A1) instead of the array with $1/2 \times 2^{30}$ components according to Eq. (8).

In addition, the summation over m in Eq. (7) coincides with the time loop of the simulation. We can add a procedure into the simulation loop to implement the discrete Fourier transformation of Eq. (7) on the fly. In this procedure, the mth term of $f(t_m)\, e^{i\omega_n t_m}$ in the summation of Eq. (7) is computed during the mth simulation step and is added sequentially to the array of $f(\omega_n)$. Therefore, there is no need to output the entire time series of $f(t_m)$ during a simulation. After multiple simulations, substituting the computed $f(\omega_n)$ into Eq. (6), and taking the average over the number of the simulations, we get $F(\omega_n)$ without storing the entire time series of $f(t_m)$ and without any lack of $f(t_m)$. The postsimulation computation to get $F(\omega_n)$ is also reduced dramatically by this algorithm.

Figure 9 shows an example of *the on-the-fly algorithm for the WKT*, where we present a schematic illustration of how to compute the frequency-domain velocity correlation function $F(\omega_n)$, which is the Fourier transform of the velocity autocorrelation function of atoms, from MD simulations. In Fig. 9(c), the peak around 3.0×10^{11} Hz is a low-energy excitation (often referred to "Boson peak"), which appears in Raman scattering, neutron scattering, x-ray scattering and simulation data [25–34]. The peak position is used to examine the wave-vector-dependent dynamic susceptibilities computed for an isotropic amorphous polyethylene in Sec. VII.

This on-the-fly algorithm is quite simple and general. Thus, we may apply the algorithm to other methods transforming the time series $f(t_m)$, such as the windowed Fourier transformation or the wavelet transformation. We can replace the green-colored procedure in Fig. 9(a) with others depending on the purposes and can do the transformation on the fly during the simulations.

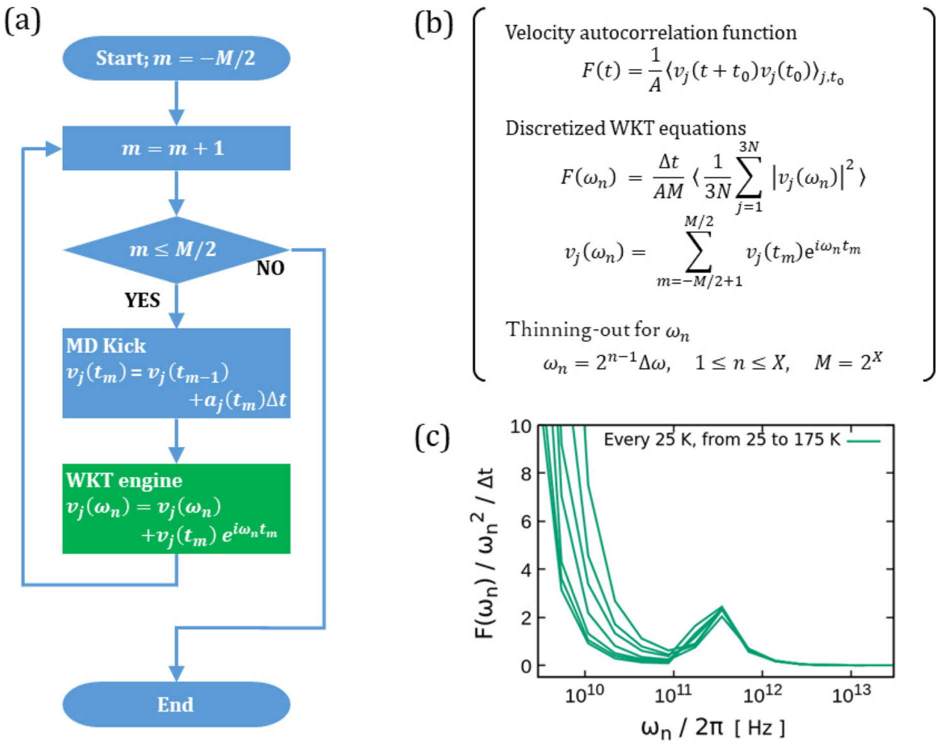

Velocity autocorrelation function

$$F(t) = \frac{1}{A}\langle v_j(t+t_0)v_j(t_0)\rangle_{j,t_0}$$

Discretized WKT equations

$$F(\omega_n) = \frac{\Delta t}{AM}\left\langle \frac{1}{3N}\sum_{j=1}^{3N} |v_j(\omega_n)|^2 \right\rangle$$

$$v_j(\omega_n) = \sum_{m=-M/2+1}^{M/2} v_j(t_m)e^{i\omega_n t_m}$$

Thinning-out for ω_n

$$\omega_n = 2^{n-1}\Delta\omega, \quad 1 \le n \le X, \quad M = 2^X$$

FIG. 9. On-the-fly algorithm for the WKT: (a) a flow chart of time loop of an MD simulation, (b) equations for computing the frequency-domain velocity correlation function $F(\omega_n)$, and (c) an example of $F(\omega_n)$ versus $\log \omega_n$. In panel (b), $v_j(t)$ is the velocity of the jth degree of freedom at time t. In the equation for $F(t)$, the angular brackets subscripted by j and t_0 $\langle \cdots \rangle_{j,t_0}$ means taking the number average over j and the long-time average over time t_0; in the equation for $F(\omega_n)$, N is the number of atoms. The angular frequency ω_n is thinned out by the equations on the last line in panel (b). When implementing the simulation of $2^{30}(>10^9)$ steps, it suffices to use $X = 30$ here. In panel (a), at the green-colored procedure named WKT engine, $v_j(t_m)\, e^{i\omega_n t_m}$ is computed at each time step and added sequentially to the array of $v_j(\omega_n)$. After multiple simulations, substituting $v_j(\omega_n)$ into the right-hand side of the equation for $F(\omega_n)$ and taking the average over the number of simulations gives the frequency-domain velocity correlation function $F(\omega_n)$. Panel (c) presents the results of an MD simulation for the united atom polyethylene; $F(\omega_n)$ computed for the low-temperature glass is plotted versus the $\log \omega_n$. The peak around 3.0×10^{11} Hz is a low-energy excitation (often referred to "Boson peak"), which appears in Raman scattering, neutron scattering, x-ray scattering, and simulation data [25–34].

APPENDIX B: DIFFERENCE BETWEEN THE EFFECTIVE ACF AND THE LONG-TIME-AVERAGED ACF

The effective ACF $F_e(t)$ of Eq. (14) is not the same as the well-known long-time-averaged ACF $F(t)$ of Eq. (11). Here we show explicitly how they differ.

When the time series of f is limited to a finite time interval from $-T/2$ to $T/2$ [as in Sec. II], the range of the time lag t between $f(t+t_0)$ and $f(t_0)$ can be up to twice as large as the time interval. Thus, the domain of the time-averaged ACF is often set to be twice as large as the time interval. Here, as per convention, we set the time domain of $F_e(t)$ and $F(t)$ to $-T < t < T$.

First, we rewrite the effective ACF $F_e(t)$ [Eq. (14)] in the single-integral form and compare it with the long-time-averaged ACF $F(t)$ [Eq. (11)]. To do this, we define a rectangular window function $W[a < t < b]$ as follows:

$$W[a < t < b] \equiv \{1, \quad a < t < b; \quad 0, \quad \text{otherwise}\}. \quad \text{(B1)}$$

We insert the window function $W[-T/2 < t' < T/2]$ into the integral of Eq. (14) and remove the limit on T from Eq. (14). However, we do not add the brackets $\langle \cdots \rangle$ for statistical averaging even after removing the limit on T, because the goal is to compare $F_e(t)$ with $F(t)$ on the planes t versus t_0 and t' versus t_0 depicted in Figs. 10 and 11, respectively. In this Appendix, Eqs. (11) and (14) are treated as not having

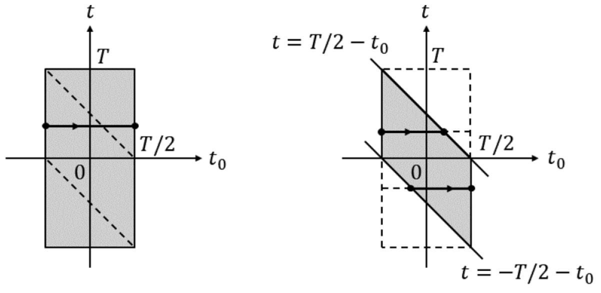

(a) Long-time averaged ACF $F(t)$ (b) Effective ACF $F_e(t)$

FIG. 10. Schematic diagrams of integration over t_0 in Eqs. (11) and (B2): (a) $F(t)$ and (b) $F_e(t)$. The integral over t_0 with a fixed t means the integration along the line segment between two filled circles.

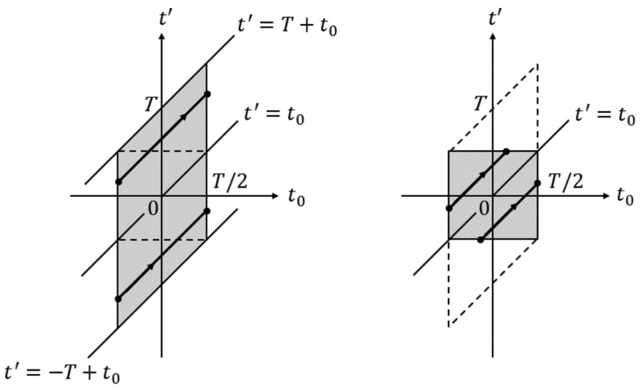

(a) Long-time averaged ACF $F(t)$ (b) Effective ACF $F_e(t)$

FIG. 11. Schematic diagrams of integration over t' and t_0 in Eqs. (B4) and (14): (a) $F(t)$ and (b) $F_e(t)$. The double integral of Eqs. (B4) and (14) over t' and t_0 means the integration along the line segment between two filled circles for a fixed t. The t value is equal to the t' value at the intercept of the line segment on the t' axis.

both the limit on T and the statistical-averaging brackets $\langle\cdots\rangle$ (the necessity to do this is explained later). Then, we split the integral over t' into two integrals of the intervals $t_0 \leqslant t' < \infty$ and $-\infty < t' \leqslant t_0$ by using the Heaviside unit step functions $\theta(t'-t_0)$ and $\theta(t_0-t')$, and we integrate them over t'. The resulting effective ACF expressed by the single integral over t_0 is

$$\begin{aligned}
F_e(t) &= \frac{1}{AT}\int_{-T/2}^{T/2} dt_0 \int_{-\infty}^{\infty} dt'\, W[-T/2 < t' < T/2] \\
&\quad \times f(t')f(t_0)\,\delta(t'-(t+t_0)) \\
&= \frac{1}{AT}\int_{-T/2}^{T/2} dt_0 \int_{-\infty}^{\infty} dt'\, [\theta(t'-t_0)+\theta(t_0-t')] \\
&\quad \times W[-T/2 < t' < T/2]\, f(t')f(t_0)\,\delta(t'-(t+t_0)) \\
&= \frac{1}{AT}[\theta(t)+\theta(-t)]\int_{-T/2}^{T/2} dt_0 \\
&\quad \times W[-T/2 < t+t_0 < T/2]\, f(t+t_0)f(t_0) \\
&= \left\{\begin{array}{ll} \frac{1}{AT}\int_{-T/2}^{T/2-t} dt_0\, f(t+t_0)f(t_0), & t>0 \\ 1, & t=0 \\ \frac{1}{AT}\int_{-T/2-t}^{T/2} dt_0\, f(t+t_0)f(t_0), & t<0 \end{array}\right\}. \qquad \text{(B2)}
\end{aligned}$$

Figure 10 shows schematic diagrams of the integration area for $F(t)$ [Eq. (11)] and $F_e(t)$ [Eq. (B2)] on the plane t versus t_0. The integral over t_0 with a fixed t means integrating along the line segment between two filled circles. Figures 10(a) and 10(b) show that the two integration areas in $F(t)$ highlighted by the dashed lines are missing in $F_e(t)$. Note that, in the last line of Eq. (B2), the integration intervals over t_0 depend on t, although the integrals are divided by the constant T. Thus, $F_e(t)$ is not a time-averaged autocorrelation function in the strict sense.

Next, we rewrite the long-time-averaged ACF $F(t)$ of Eq. (11) in the double-integral form, similar to $F_e(t)$ of Eq. (14). To restrict the time range of t to $-T < t < T$, we write $f(t+t_0)$ with the window function $W[-T < t < T]$ as

$$\begin{aligned}
f(t+t_0) &= W[-T < t < T] \\
&\quad \times \int_{-\infty}^{\infty} dt'\, f(t')\,\delta(t'-(t+t_0)). \qquad \text{(B3)}
\end{aligned}$$

Substituting Eq. (B3) into Eq. (11) gives

$$\begin{aligned}
F(t) &= \frac{1}{AT}\int_{-T/2}^{T/2} dt_0 \int_{-\infty}^{\infty} dt' \\
&\quad \times W[-T < t'-t_0 < T]\, f(t')f(t_0)\,\delta(t'-(t+t_0)) \\
&= \frac{1}{AT}\int_{-T/2}^{T/2} dt_0 \int_{-T+t_0}^{T+t_0} dt' f(t')f(t_0)\,\delta(t'-(t+t_0)). \qquad \text{(B4)}
\end{aligned}$$

Figure 11 shows schematic diagrams of the integration areas of $F(t)$ [Eq. (B4)] and $F_e(t)$ [Eq. (14)] on the plane t' versus t_0. The vertical axes are changed from t in Fig. 10 to t' in Fig. 11. In Fig. 11, the double integral of Eqs. (B4) and (14) over t' and t_0 with the δ function $\delta(t'-(t+t_0))$ means that $f(t')f(t_0)$ is integrated along the line segment between two filled circles for a fixed t; the t value is equal to the t' value at the intercept of the line segment on the t' axis. Figure 11 shows that two integration areas highlighted by the dashed lines in $F(t)$ are missing in $F_e(t)$, which is the same as in Fig. 10.

From the discussion, we can see that the integration areas for $F(t)$ and $F_e(t)$ differ, which comes from the assumption for the domain of $f(t+t_0)$ in $F_e(t)$ to be restricted to $-T/2 < t+t_0 < T/2$ [see Eq. (13)]. Equating the $F(t)$ and $F_e(t)$ means ignoring the highlighted area with the dashed lines in Figs. 10(a) and 11(a), which links to the requirements for the WKT to hold, discussed in Appendix C.

If we add the statistical-averaging brackets $\langle\cdots\rangle$ to the last line of Eq. (B2), for example, the integration variable t_0 disappears:

$$\begin{aligned}
F_e(t) &= \frac{1}{AT}\int_{-T/2}^{T/2-t} dt_0\, \langle f(t+t_0)f(t_0)\rangle \\
&= \frac{1}{AT}\left(\int_{-T/2}^{T/2-t} dt_0\right)\langle f(t)f(0)\rangle \\
&= \frac{1}{AT}(T-t)\langle f(t)f(0)\rangle, \quad \text{for } t>0, \qquad \text{(B5)}
\end{aligned}$$

where $\langle f(t+t_0)f(t_0)\rangle = \langle f(t)f(0)\rangle$ is used. As a result, we can no longer compare the effective ACF $F_e(t)$ with the long-time-averaged ACF $F(t)$ on the planes t versus t_0 and t' versus t_0, as done in Figs. 10 and 11. Thus, the brackets were not added to the ACFs even after removing the limit on T.

APPENDIX C: REQUIREMENT FOR WKT

In this Appendix, we derive the requirement for the infinite-continuous WKT [Eq. (2)]. We define a time-averaged ACF $F_1(t)$ over the highlighted areas outlined by dashed lines in Figs. 10 and 11. For $0 < t < T/2$, $F_1(t)$ is

$$\begin{aligned} F_1(t) &\equiv \frac{1}{At}\int_{T/2-t}^{T/2} dt_0\, f(t+t_0)f(t_0) \\ &= \frac{1}{At}\int_{-T/2}^{T/2} dt_0 \int_{T/2}^{T+t_0} dt' \\ &\quad \times f(t')f(t_0)\,\delta(t'-(t+t_0)), \end{aligned} \tag{C1}$$

and for $-T/2 < t < 0$,

$$\begin{aligned} F_1(t) &\equiv \frac{1}{A(-t)}\int_{-T/2}^{-T/2-t} dt_0\, f(t+t_0)f(t_0) \\ &= \frac{1}{A(-t)}\int_{-T/2}^{T/2} dt_0 \int_{-T+t_0}^{-T/2} dt' \\ &\quad \times f(t')f(t_0)\,\delta(t'-(t+t_0)). \end{aligned} \tag{C2}$$

The relation between $F(t)$ of Eq. (B4), $F_e(t)$ of Eq. (B2), and $F_1(t)$ is

$$\begin{aligned} F_e(t) &= \begin{Bmatrix} F(t) - \frac{t}{T}F_1(t), & t > 0 \\ 1, & t = 0 \\ F(t) + \frac{t}{T}F_1(t), & t < 0 \end{Bmatrix} \\ &= F(t) - \mathrm{sgn}(t)\frac{t}{T}F_1(t), \end{aligned} \tag{C3}$$

where $\mathrm{sgn}(t) \equiv \theta(t) - \theta(-t)$ is the sign function, and $\theta(t)$ is the unit step function defined in Eq. (18). When we add the brackets $\langle \cdots \rangle$ to Eq. (C3), $\langle F_1(t)\rangle$ on the right-hand side becomes equal to $\langle F(t)\rangle$:

$$\begin{aligned} \langle F_1(t)\rangle &= \frac{1}{At}\int_{T/2-t}^{T/2} dt_0\, \langle f(t+t_0)f(t_0)\rangle \\ &= \frac{1}{At}\left(\int_{T/2-t}^{T/2} dt_0\right)\langle f(t)f(0)\rangle \\ &= \frac{1}{A}\langle f(t)f(0)\rangle = F(t), \text{ for } t > 0, \end{aligned} \tag{C4}$$

where, according to Eq. (1), we have removed the brackets from $F(t)$ in the last line of Eq. (C4). Equation (C3) then becomes

$$\langle F_e(t)\rangle = F(t) - \mathrm{sgn}(t)\frac{t}{T}F(t). \tag{C5}$$

Implementing the Fourier integrals on both sides of Eq. (C5) with the integration intervals $0 < t < T$ and $-T < t < 0$ gives

$$\begin{aligned} &\int_0^T dt\, \langle F_e(t)\rangle\, e^{i\omega t} \\ &\quad = \int_0^T dt\, F(t)\, e^{i\omega t} - \frac{1}{T}\int_0^T dt\, tF(t)\, e^{i\omega t} \end{aligned} \tag{C6}$$

and

$$\begin{aligned} &\int_{-T}^0 dt\, \langle F_e(t)\rangle\, e^{i\omega t} \\ &\quad = \int_{-T}^0 dt\, F(t)\, e^{i\omega t} + \frac{1}{T}\int_{-T}^0 dt\, tF(t)\, e^{i\omega t}. \end{aligned} \tag{C7}$$

If we take the limit $T \to \infty$ in Eqs. (C6) and (C7), the second terms on the right-hand sides go to zero provided the Fourier integrals of $tF(t)$ converge to finite values for arbitrary ω. In addition, as long as the first terms converge to finite values for arbitrary ω when $T \to \infty$, combining Eqs. (C6) and (C7) gives the following relation:

$$\int_{-\infty}^{\infty} dt\, F_e(t)\, e^{i\omega t} = \int_{-\infty}^{\infty} dt\, F(t)\, e^{i\omega t}. \tag{C8}$$

Having taken the limit $T \to \infty$, we make the assumption of ergodicity, so the brackets are removed from $F_e(t)$ on the left-hand side of Eq. (C8). Equation (C8) corresponds to the WKT Eq. (2); the left-hand side and right-hand side are the power spectral density $I(\omega)$ and the Fourier transform of the ACF $F(\omega)$, respectively.

Based on the discussion above, the WKT requires the convergences of the following Fourier integrals to finite values for arbitrary ω:

$$\int_0^{\infty} dt\, F(\pm t)\, e^{\pm i\omega t} \quad \text{and} \quad \int_0^{\infty} dt\, tF(\pm t)\, e^{\pm i\omega t}. \tag{C9}$$

This requirement is the same as that given in Ref. [9]. The second terms omitted in Eqs. (C6) and (C7) come from the highlighted areas outlined by dashed lines in Figs. 10 and 11. Thus, eliminating the unnecessary terms translates into ignoring these highlighted areas.

APPENDIX D: CONVERGENCE VALUE OF THE SUMMATION IN EQ. (38) FOR THE DEBYE RELAXATION MODEL

As written in Sec. V, knowing the convergence value of the summation in Eq. (38) is difficult without using a specific model for the ACF $F(t_k) = \langle f(t_k)f(0)\rangle$. In this Appendix, we assume as an example that the ACF $F(t_k)$ can be reproduced by the Debye relaxation function, and we confirm that the summation converges to a finite negative value in this case.

The discrete Fourier-Laplace transformation for $F(t_k)$ is written as

$$\begin{aligned} F^+(\omega_n) &= \Delta t \sum_{k=-M/2+1}^{M/2} \theta_k\, F(t_k)\, e^{i\omega_n t_k} \\ &= \Delta t\left(\sum_{k=0}^{M/2} F(t_k)\, e^{i\omega_n t_k} - \frac{1}{2}\right), \end{aligned} \tag{D1}$$

where θ_k is the discretized unit step function of Eq. (31). Differentiating Eq. (D1) with respect to ω_n gives

$$\frac{dF^+(\omega_n)}{d\,\omega_n} = i\Delta t\sum_{k=0}^{M/2} F(t_k)\, t_k\, e^{i\omega_n t_k}. \tag{D2}$$

When setting $\omega_n = \pi/\Delta t$ in Eq. (D2), the summation on the right-hand side of Eq. (D2) corresponds to the summation in Eq. (38) because $t_k = k\Delta t$.

Next, we assume that the ACF can be written by the Debye relaxation function with a relaxation time τ as $F(t_k) = e^{-t_k/\tau}$, and we substitute this into Eq. (D1):

$$F^{+}(\omega_n) = \Delta t\left(\sum_{k=0}^{M/2} e^{-t_k/\tau}\, e^{i\omega_n t_k} - \frac{1}{2}\right)$$
$$= \Delta t\left(\sum_{k=0}^{M/2} e^{zk} - \frac{1}{2}\right) = \Delta t\left(\frac{1-e^{z(M/2+1)}}{1-e^{z}} - \frac{1}{2}\right), \tag{D3}$$

where z is

$$z = (-1/\tau + i\omega_n)\Delta t. \tag{D4}$$

In Eq. (D3), we see $F^{+}(\omega_n) \to 0$ at the Nyquist frequency $\omega_n = \pi/\Delta t$ in the case $\Delta t \ll \tau \ll T/2$, where $T = M\Delta t$ from Eq. (8).

Differentiating Eq. (D3) with respect to ω_n gives

$$\frac{dF^{+}(\omega_n)}{d\,\omega_n} = \frac{dz}{d\,\omega_n}\frac{dF^{+}(\omega_n)}{dz}$$
$$= i(\Delta t)^2 \frac{e^{z}}{(1-e^{z})^2}$$
$$\times\left\{-\left[\frac{M}{2}(1-e^{z})+1\right]e^{zM/2}+1\right\}. \tag{D5}$$

Substituting $\omega_n = \pi/\Delta t$ into Eq. (D5) through Eq. (D4), and combining this with Eq. (D2), we get the following form for the summation in Eq. (38):

$$\sum_{k=0}^{M/2} F(t_k)\, t_k\, (-1)^k = \frac{1}{i\Delta t}\frac{dF^{+}(\omega_n)}{d\,\omega_n}\bigg|_{\omega_n=\pi/\Delta t}$$
$$= \Delta t\frac{-e^{-\Delta t/\tau}}{(1+e^{-\Delta t/\tau})^2}$$
$$\times\left\{-\left[\frac{M}{2}(1+e^{-\Delta t/\tau})+1\right](-1)^{M/2}\right.$$
$$\left.\times\, e^{-T/2\tau}+1\right\}. \tag{D6}$$

On the right-hand side in Eq. (D6), the first term in the curly brackets can be ignored when $\tau \ll T/2$, and we thus obtain

$$\sum_{k=0}^{M/2} F(t_k) t_k\, (-1)^k \cong \Delta t\frac{-e^{-\Delta t/\tau}}{(1+e^{-\Delta t/\tau})^2}$$
$$\to -0.25\Delta t, \quad \text{for} \quad \Delta t \ll \tau. \tag{D7}$$

From Eqs. (D6) and (D7), we confirm that the summation in Eq. (38) converges to the finite negative value $-0.25\Delta t$ for $\Delta t \ll \tau \ll T/2$ when using the Debye relaxation model.

APPENDIX E: DISCRETIZED WKT-FLT EQUATION FOR DYNAMIC STRUCTURE FACTOR AND WAVE-VECTOR-DEPENDENT DYNAMIC SUSCEPTIBILITY

In this Appendix, starting from the van Hove time-space density correlation function for classical systems [24], we derive the discretized WKT-FLT equations for the dynamic structure factor and the wave-vector-dependent dynamic susceptibility [9,19]. For simplicity, we call these the frequency-domain density correlation function and response function, respectively.

The van Hove time-space density correlation function $G(\mathbf{r}, t)$ is defined as follows:

$$G(\mathbf{r}, t) \equiv \frac{1}{N}\left\langle \sum_{j=1}^{N}\sum_{k=1}^{N} \delta(\mathbf{r}+\mathbf{r}_j(0)-\mathbf{r}_k(t)) \right\rangle$$
$$= \frac{1}{\rho}\langle\, \rho(\mathbf{r}, t)\, \rho(\mathbf{0}, 0)\,\rangle, \tag{E1}$$

where $\mathbf{r}$ is a position vector, t is time, N is the number of atoms, and $\mathbf{r}_j(t)$ is the position of atom j at time t. The constant $\rho \equiv N/V$ is the average number density, where V is the sample volume. The first form may be expressed in the second form [21] by using the expression for the density:

$$\rho(\mathbf{r}, t) = \sum_{j=1}^{N} \delta(\mathbf{r}-\mathbf{r}_j(t)). \tag{E2}$$

We replace the statistical average $\langle\cdots\rangle$ with the long-time average and space average $\langle\cdots\rangle_{t_0,\mathbf{r}_0}$ by assuming ergodicity:

$$\langle\cdots\rangle_{t_0} = \lim_{T\to\infty}\frac{1}{T}\int_{-T/2}^{T/2} dt_0\,(\cdots) \tag{E3a}$$

and

$$\langle\cdots\rangle_{\mathbf{r}_0} = \frac{1}{V}\int_{V} d\mathbf{r}_0\,(\cdots)$$
$$= \lim_{L\to\infty}\frac{1}{L^3}\int_{-\mathbf{L}/2}^{\mathbf{L}/2} d\mathbf{r}_0\,(\cdots), \tag{E3b}$$

where the integration over the volume V in the first step of Eq. (E3b) means that the integration of the position $\mathbf{r}_0$ encompasses all the sample material. Considering the application of the WKT-FLT to molecular simulations, we use the second form of Eq. (E3b), and we use a cubic simulation box with the periodic boundaries: $\rho(\mathbf{r}\pm\mathbf{L}, t) = \rho(\mathbf{r}, t)$, where $\mathbf{L} = (L, L, L)$.

Using Eqs. (E3a) and (E3b), $G(\mathbf{r}, t)$ takes the form

$$G(\mathbf{r}, t) = \frac{1}{\rho}\langle\, \rho(\mathbf{r}+\mathbf{r}_0, t+t_0)\, \rho(\mathbf{r}_0, t_0)\,\rangle_{t_0,\mathbf{r}_0}$$
$$= \lim_{T,L\to\infty}\frac{1}{TN}\int_{-T/2}^{T/2} dt_0 \int_{-\mathbf{L}/2}^{\mathbf{L}/2} d\mathbf{r}_0$$
$$\times\, \rho(\mathbf{r}+\mathbf{r}_0, t+t_0)\, \rho(\mathbf{r}_0, t_0), \tag{E4}$$

where N is included in the limit on L because N depends on L for a constant ρ. In Eq. (E4) the convolution over position $\mathbf{r}_0$ is written in the same way as the convolution over time t_0. However, they have different meanings when the limits on T and L are removed. For position, we impose the periodicity $\rho(\mathbf{r}\pm\mathbf{L}, t) = \rho(\mathbf{r}, t)$ in space with the periodic boundaries, so that the value beyond the boundaries can be replaced with the appropriate value from inside the simulation box. Conversely, for time, $\rho(\mathbf{r}, t)$ is limited to the fixed time range $|t| < T/2$, and no periodicity applies for t. We thus cannot apply the same replacement strategy for time as for position. Therefore, we must pay attention to the requirements of the

WKT (see Appendixes B and C and Sec. VIII) in the case of time, whereas this is unnecessary in the case of space.

In Eq. (E4) we thus restrict the time domain of $\rho(\mathbf{r}+\mathbf{r}_0, t+t_0)$ to $-T/2 < t+t_0 < T/2$, and impose the periodicity $\rho(\mathbf{r}\pm\mathbf{L}, t) = \rho(\mathbf{r}, t)$ as follows:

$$\begin{aligned}\rho(\mathbf{r}+\mathbf{r}_0\pm\mathbf{L}, t+t_0) &= \rho(\mathbf{r}+\mathbf{r}_0, t+t_0)\\ &= \int_{-T/2}^{T/2} dt' \int_{-\mathbf{L}/2}^{\mathbf{L}/2} d\mathbf{r}'\,\rho(\mathbf{r}', t')\\ &\quad\times\delta(\mathbf{r}'-(\mathbf{r}+\mathbf{r}_0))\,\delta(t'-(t+t_0)).\end{aligned}\tag{E5}$$

Substituting Eq. (E5) into Eq. (E4), we obtain the effective time-space density correlation function $G_{\mathrm{e}}(\mathbf{r}, t)$:

$$\begin{aligned}G(\mathbf{r}, t) &\cong G_{\mathrm{e}}(\mathbf{r}, t)\\ &= \lim_{T,L\to\infty}\frac{1}{TN}\int_{-T/2}^{T/2} dt_0 \int_{-T/2}^{T/2} dt' \int_{-\mathbf{L}/2}^{\mathbf{L}/2} d\mathbf{r}_0 \int_{-\mathbf{L}/2}^{\mathbf{L}/2} d\mathbf{r}'\\ &\quad\times\rho(\mathbf{r}', t')\,\rho(\mathbf{r}_0, t_0)\,\delta(\mathbf{r}'-(\mathbf{r}+\mathbf{r}_0))\delta(t'-(t+t_0)).\end{aligned}\tag{E6}$$

Next, substituting Eq. (E6) into Eq. (40), we get the effective function $\chi_{\mathrm{e}}(\mathbf{r}, t)$:

$$\begin{aligned}\chi(\mathbf{r}, t) &\cong \chi_{\mathrm{e}}(\mathbf{r}, t)\\ &= -\lim_{T,L\to\infty}\frac{1}{TN}\int_{-T/2}^{T/2} dt_0 \int_{-T/2}^{T/2} dt' \int_{-\mathbf{L}/2}^{\mathbf{L}/2} d\mathbf{r}_0\\ &\quad\times\int_{-\mathbf{L}/2}^{\mathbf{L}/2} d\mathbf{r}'\dot{\rho}(\mathbf{r}', t')\,\rho(\mathbf{r}_0, t_0)\,\delta(\mathbf{r}'-(\mathbf{r}+\mathbf{r}_0))\\ &\quad\times\delta(t'-(t+t_0)).\end{aligned}\tag{E7}$$

Note that $\chi(\mathbf{r}, t)$ and $\chi_{\mathrm{e}}(\mathbf{r}, t)$ are response functions in time t and are correlation functions in space $\mathbf{r}$.

By implementing the Fourier transformation in space and the Fourier-Laplace transformation in time for $G(\mathbf{r}, t)$ and $\chi(\mathbf{r}, t)$, we obtain the coherent (full-correlation) parts of the frequency-domain density correlation function $S^{+}(\mathbf{q}, \omega)$ and response function $\chi^{+}(\mathbf{q}, \omega)$, respectively, where $\mathbf{q}$ is the wave vector:

$$\begin{aligned}S^{+}(\mathbf{q}, \omega) &= \int_{0}^{\infty} dt \int_{V} d\mathbf{r}\, G(\mathbf{r}, t)\, e^{-i(\mathbf{q}\cdot\mathbf{r}-\omega t)}\\ &= \int_{-\infty}^{\infty} dt\,\theta(t) \int_{V} d\mathbf{r}\, G(\mathbf{r}, t)\, e^{-i(\mathbf{q}\cdot\mathbf{r}-\omega t)}\end{aligned}\tag{E8}$$

and

$$\begin{aligned}\chi^{+}(\mathbf{q}, \omega) &= \int_{0}^{\infty} dt \int_{V} d\mathbf{r}\, \chi(\mathbf{r}, t)\, e^{-i(\mathbf{q}\cdot\mathbf{r}-\omega t)}\\ &= \int_{-\infty}^{\infty} dt\,\theta(t) \int_{V} d\mathbf{r}\, \chi(\mathbf{r}, t)\, e^{-i(\mathbf{q}\cdot\mathbf{r}-\omega t)}.\end{aligned}\tag{E9}$$

Substituting $G_{\mathrm{e}}(\mathbf{r}, t)$ and $\chi_{\mathrm{e}}(\mathbf{r}, t)$ into Eqs. (E8) and (E9) in the places of $G(\mathbf{r}, t)$ and $\chi(\mathbf{r}, t)$, respectively, we get the WKT-FLT equations for $S^{+}(\mathbf{q}, \omega)$ and $\chi^{+}(\mathbf{q}, \omega)$:

$$\begin{aligned}S^{+}(\mathbf{q}, \omega) &= \lim_{T,L\to\infty}\frac{1}{TN}\sum_{j=1}^{N}\sum_{k=1}^{N}\int_{-T/2}^{T/2} dt_0 \int_{t_0}^{T/2} dt'\\ &\quad\times\rho_j(\mathbf{q}, t')\,\rho_k^{*}(\mathbf{q}, t_0)\, e^{i\omega(t'-t_0)}\\ &= \lim_{T,L\to\infty}\frac{1}{TN}\int_{-T/2}^{T/2} dt_0\\ &\quad\times\int_{t_0}^{T/2} dt'\rho(\mathbf{q}, t')\,\rho^{*}(\mathbf{q}, t_0)\, e^{i\omega(t'-t_0)}\end{aligned}\tag{E10}$$

and

$$\begin{aligned}\chi^{+}(\mathbf{q}, \omega) &= -\lim_{T,L\to\infty}\frac{1}{TN}\sum_{j=1}^{N}\sum_{k=1}^{N}\int_{-T/2}^{T/2} dt_0 \int_{t_0}^{T/2} dt'\\ &\quad\times[-i\mathbf{q}\cdot\dot{\mathbf{r}}_j(t')]\rho_j(\mathbf{q}, t')\,\rho_k^{*}(\mathbf{q}, t_0)\, e^{i\omega(t'-t_0)}\\ &= -\lim_{T,L\to\infty}\frac{1}{TN}\int_{-T/2}^{T/2} dt_0\\ &\quad\times\int_{t_0}^{T/2} dt'\dot{\rho}(\mathbf{q}, t')\,\rho^{*}(\mathbf{q}, t_0)\, e^{i\omega(t'-t_0)},\end{aligned}\tag{E11}$$

where $\rho_j(\mathbf{q}, t)$ is the complex scattering amplitude of atom j:

$$\rho_j(\mathbf{q}, t) = \int_{-\mathbf{L}/2}^{\mathbf{L}/2} d\mathbf{r}\,\delta(\mathbf{r}-\mathbf{r}_j(t))\, e^{-i\mathbf{q}\cdot\mathbf{r}} = e^{-i\mathbf{q}\cdot\mathbf{r}_j(t)}.\tag{E12}$$

The complex scattering amplitude of the whole system $\rho(\mathbf{q}, t)$ is the Fourier transform of the density $\rho(\mathbf{r}, t)$ [Eq. (E2)] in space and is given by the superposition of $\rho_j(\mathbf{q}, t)$:

$$\begin{aligned}\rho(\mathbf{q}, t) &= \int_{-\mathbf{L}/2}^{\mathbf{L}/2} d\mathbf{r}\,\rho(\mathbf{r}, t)\, e^{-i\mathbf{q}\cdot\mathbf{r}}\\ &= \sum_{j=1}^{N} e^{-i\mathbf{q}\cdot\mathbf{r}_j(t)} = \sum_{j=1}^{N}\rho_j(\mathbf{q}, t).\end{aligned}\tag{E13}$$

By replacing ω with $\omega_n = 2\pi n/T$, removing the limits on T and L, and adding the brackets $\langle\cdots\rangle$, Eqs. (E10) and (E11) are modified to the forms including the Heaviside unit step function $\theta(t'-t_0)$ of Eq. (18). In addition, they are discretized by replacing the integrals with the summations using the discretized unit step function θ_k of Eq. (31). After discretization, we get the following forms of the discretized WKT-FLT equations for the coherent (full-correlation) parts of the frequency-domain density correlation and response functions:

$$\begin{aligned}S^{+}(\mathbf{q_h}, \omega_n) &= \frac{\Delta t}{MN}\left\langle\sum_{m=-M/2+1}^{M/2}\rho(\mathbf{q_h}, t_m)\, e^{i\omega_n t_m}\right.\\ &\quad\left.\times\sum_{l=-M/2+1}^{m}\rho^{*}(\mathbf{q_h}, t_l)\, e^{-i\omega_n t_l}\right\rangle - \frac{\Delta t}{2}S(\mathbf{q_h})\end{aligned}\tag{E14}$$

and

$$\chi^{+}(\mathbf{q_h},\omega_n) = -\frac{\Delta t}{MN}\left\langle \sum_{m=-M/2+1}^{M/2} \dot{\rho}(\mathbf{q_h},t_m)\, e^{i\omega_n t_m} \times \sum_{l=-M/2+1}^{m} \rho^{*}(\mathbf{q_h},t_l)\, e^{-i\omega_n t_l} \right\rangle, \tag{E15}$$

where the second term in Eq. (E14) is the correction term, and $S(\mathbf{q_h})$ is the discretized static structure factor:

$$S(\mathbf{q_h}) = \frac{1}{MN}\left\langle \sum_{l=-M/2+1}^{M/2} \rho(\mathbf{q_h},t_l)\, \rho^{*}(\mathbf{q_h},t_l) \right\rangle. \tag{E16}$$

In Eqs. (E14)–(E16), the wave vector $\mathbf{q}$ is discretized as

$$\mathbf{q_h} = (h_x\Delta q, h_y\Delta q, h_z\Delta q), \quad \Delta q = \frac{2\pi}{L}, \quad h_x, h_y \text{ and } h_z = 1, 2, 3, \ldots. \tag{E17}$$

The discretized forms of the incoherent (self-correlation) parts of the frequency-domain density correlation function $S_{\mathrm{s}}^{+}(\mathbf{q_h},\omega_n)$ and response function $\chi_{\mathrm{s}}^{+}(\mathbf{q_h},\omega_n)$ are obtained by introducing the Kronecker delta $\delta_{j,k}$ into the double summations of Eqs. (E14)–(E16) as follows:

$$S_{\mathrm{s}}^{+}(\mathbf{q_h},\omega_n) = \frac{\Delta t}{MN}\left\langle \sum_{j=1}^{N}\sum_{m=-M/2+1}^{M/2} \rho_j(\mathbf{q_h},t_m)\, e^{i\omega_n t_m} \times \sum_{l=-M/2+1}^{m} \rho_j^{*}(\mathbf{q_h},t_l)\, e^{-i\omega_n t_l} \right\rangle - \frac{\Delta t}{2} \tag{E18}$$

and

$$\chi_{\mathrm{s}}^{+}(\mathbf{q_h},\omega_n) = -\frac{\Delta t}{MN}\left\langle \sum_{j=1}^{N}\sum_{m=-M/2+1}^{M/2} \dot{\rho}_j(\mathbf{q_h},t_m)\, e^{i\omega_n t_m} \times \sum_{l=-M/2+1}^{m} \rho_j^{*}(\mathbf{q_h},t_l)\, e^{-i\omega_n t_l} \right\rangle. \tag{E19}$$

Equations (E15) and (E19) are used to compute the $\chi^{+}(\mathbf{q_h},\omega_n)$ and $\chi_{\mathrm{s}}^{+}(\mathbf{q_h},\omega_n)$ shown in Figs. 6 and 7.

APPENDIX F: SIMULATION OUTLINES

This Appendix shows the outlines of the simulations for the application examples in Sec. VII. Throughout this research, the codes for the MD simulations, the WKT engine and the WKT-FLT engine (see the flow charts in Figs. 4 and 9) were written with FORTRAN 90, and they were compiled by GNU FORTRAN compiler. We use the velocity Verlet algorithm to integrate equations of motion. The velocity-scaling thermostat and weak coupling barostat [57] are used for the cooling simulations. For the NPT constant simulations, the Nose-Hoover thermostat [58,59] and the Andersen barostat [60] are used.

1. MD simulations for the isotropic amorphous polyethylene

This subsection explains mainly the simulations to compute the results presented in Figs. 6 and 7 of Sec. VII A. The other results of the isotropic amorphous polyethylene model, presented repeatedly in this paper (Figs. 1, 3, 5, and 9), are also computed using the same molecular model with the same way as shown in this subsection.

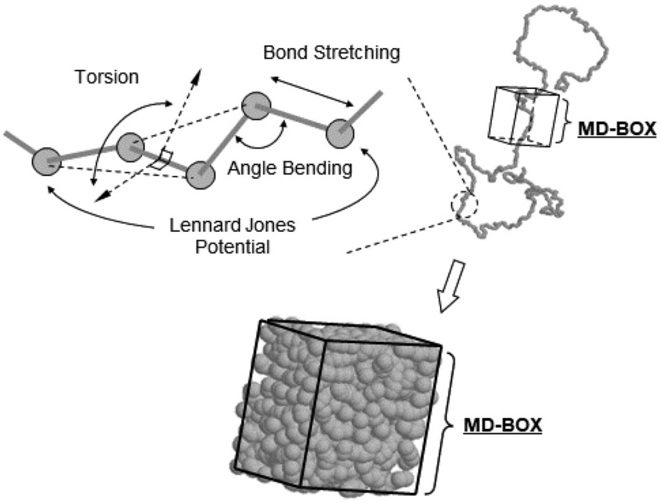

FIG. 12. Schematic picture of the united atom polyethylene model and the MD box with 3D periodic boundaries.

We employ the united atom polyethylene model (Fig. 12). The force fields are the same in our previous research [36], where the Mondello and Grest united-atom model [61] is combined with the bond stretching potential used by the Rigby and Roe [37].

First, we make an initial configuration [62] and implement an NPT constant simulation (800 K, 1 atm) for 1 ns to obtain the relaxed configuration. The system is then cooled from 800 K to the target temperatures with a cooling rate 200 K/ns under a constant pressure 1 atm (Fig. 13). Next, at a target temperature, we perform three successive simulations under NPT, NVE and NVE constant conditions for 1.4 ns each. The NPT constant simulation reproduces the relaxed state at the temperature and pressure after cooling. The subsequent NVE simulation eliminates the effect of the separation of the thermostat and barostat from the system. During the final NVE simulation, the wave-vector-dependent dynamic susceptibilities [Eqs. (E15) and (E19)] are computed by using the on-the-fly algorithm for the thinned-out WKT-FLT (Fig. 4). We implement the same simulations 10 times at each temperature and take the average over the number of the simulations. Finally, we obtain Figs. 6 and 7.

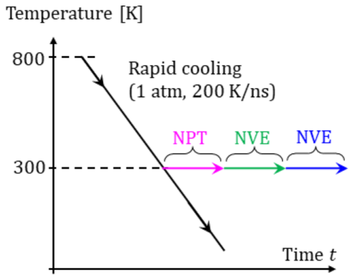

FIG. 13. Schematic diagram of the simulation, where the target temperature is 300 K.

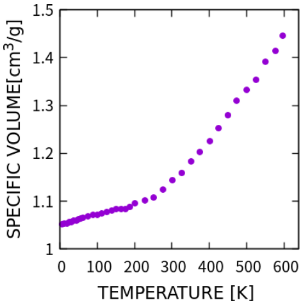

FIG. 14. Specific volume versus temperature in the isotropic amorphous polyethylene model. The slope changes between 200 and 300 K, where the system is in the melting state above 300 K and is in the glassy state below 200 K. The glass transition occurs between 200 and 300 K.

Figure 14 plots the specific volume versus temperature. The specific volume decreases with decreasing temperature, where we can observe no indication of the crystallization. Conversely, the slope changes around the temperatures from 200 K to 300 K. From this result, we consider that the glass transition occurs around these temperatures. However, it is difficult to determine the precise transition temperature from Fig. 14.

Figure 15 shows temperature changes of static structure in real space and reciprocal space for the isotropic amorphous polyethylene model: (a) radial distribution function $g(r)$ and (b) static structure factor $S(q_h)$. In Fig. 15(a), the peaks coming from the single trans conformation (t), the single ±gauche conformation (±g) [see Fig. 8(b)] and their sequences become distinct with cooling. In Fig. 15(b), the first peak position $q_{1\text{st}}$ of $S(q_h)$ shifts from 1.8 nm^{-1} to 2.4 nm^{-1} as the temperature decreases.

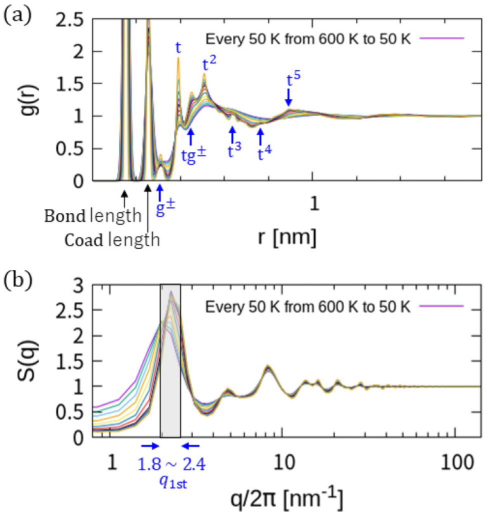

FIG. 15. Temperature changes of static structure in real space and reciprocal space for the isotropic amorphous polyethylene model: (a) radial distribution function $g(r)$ and (b) static structure factor $S(q_h)$. In panel (a), the peaks coming from the single trans conformation (t), the single ±gauche conformation (±g) (see panel (b) in Fig. 8) and their sequences become distinct with cooling. In panel (b), the first peak position $q_{1\text{st}}$ of $S(q_h)$ shifts from 1.8 nm^{-1} to 2.4 nm^{-1} as the temperature decreases.

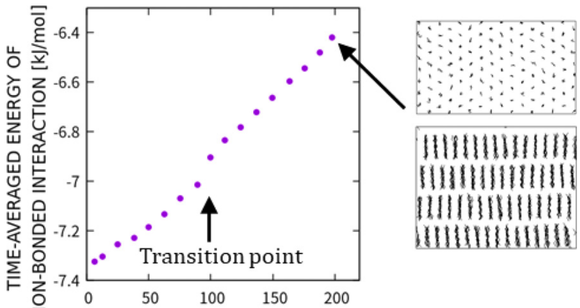

FIG. 16. Time-averaged energy of nonbonded interaction versus temperature in the n-octane crystal model. We also present the snapshots along (upper) and perpendicular to (lower) the c axis of the unit cell (the averaged direction of the molecular axes) at 200 K, where the upper snapshot shows the first layer only. The curve is discontinuous around 100 K, where the solid-solid phase transition from the high-temperature rotator phase to the low-temperature phase occurs.

These results tell us that the polymer chain tends partially to stretch with decreasing temperature, although the packing between the atoms becomes dense. This is the "frustration" in the isotropic amorphous polyethylene near the glass transition point. The frustration is supposed to be one of the causes of the glass transition [63,64] and gives rise to the thermal fluctuation of the order parameters around the transition point [35].

2. MD simulations for the *n*-octane crystal

This subsection explains the simulations presented in Sec. VII B.

We employ the united atom n-octane (C_8H_{18}) model with the force fields used by Rigby and Roe [36]. We made an initial crystal structure as follows. Two n-octane molecules are placed in an orthorhombic unit cell with the lattice constants of $a = 0.740$ nm, $b = 0.493$ nm and $c = 1.00$ nm. Four layers consisting of 8×16 unit cells in each are stacked in an MD box with 3D periodic boundaries.

Similar as in the preceding subsection, the initial crystal structure is relaxed with an NPT constant simulation (200 K and 1 atm) for 2 ns, and then the system is cooled to the target temperatures with a cooling rate 200 K/ns. Next, three successive simulations are performed under NPT, NVE and NVE constant conditions for 1.4 ns each. During the final NVE simulation at a target temperature, the frequency-domain response functions of the orientation vectors (Fig. 8) are computed by using the on-the-fly algorithm for the thinned-out WKT-FLT. Taking the average over four simulations, we get the results shown in Fig. 8.

Figure 16 plots the time-averaged energy of the nonbonded interaction versus temperature. Because the nonbonded energy is sensitive when the system goes through the first-order phase transition point in the MD simulations [65,66], here we show the figure of the nonbonded energy versus temperature instead of the free energy versus temperature. In this model, the nonbonded interaction is reproduced by the Lennard-Jones potential. The energy value decreases with decreasing temperature. The curve is discontinuous around 100 K, where the solid-solid phase transition from the high temperature rotator phase to the low-temperature phase occurs. However, as well known, the most stable herringbone packing structure in the low-temperature phase cannot be reproduced by the united atom molecular model [41]. The resulting crystal structure of this simulation is different from the ideal structure (not shown).

[1] N. Wiener, Generalized harmonic analysis, Acta Math. **55**, 117 (1930).

[2] A. Khintchine, Korrelationstheorie der stationären stochastischen Prozesse, Math. Ann. **109**, 604 (1934).

[3] J. S. Bendat and A. G. Piersol, *Random Data: Analysis and Measurement Procedures*, 4th ed., Wiley Series in Probability and Statistics(John Wiley & Sons, Hoboken, NJ, 2010).

[4] H. Nyquist, Thermal agitation of electric charge in conductors, Phys. Rev. **32**, 110 (1928).

[5] R. Kubo, The fluctuation-dissipation theorem, Rep. Prog. Phys. **29**, 306 (1966).

[6] M. S. Green, Markoff random processes and the statistical mechanics of time-dependent phenomena, J. Chem. Phys. **20**, 1281 (1952).

[7] M. S. Green, Markoff random processes and the statistical mechanics of time-dependent phenomena. II. Irreversible processes in fluids, J. Chem. Phys. **22**, 398 (1954).

[8] R. Kubo, Statistical mechanical theory of irreversible processes. I. General theory and simple applications to magnetic and conduction problems, J. Phys. Soc. Jpn. **12**, 570 (1957).

[9] R. Kubo, M. Toda, and N. Hashitsume, *Statistical Physics II: Nonequilibrium Statistical Mechanics*, Springer Series in Solid-State Sciences, 2nd ed. (Springer-Verlag, Berlin, 1998), Vol. 31.

[10] T. Hasegawa and Y. Tanimura, A polarizable water model for intramolecular and intermolecular vibrational spectroscopies, J. Phys. Chem. B **115**, 5545 (2011).

[11] M. Thomas, M. Brehm, R. Fligg, P. Vöhringer, and B. Kirchner, Computing vibrational spectra from *ab initio* molecular dynamics, Phys. Chem. Chem. Phys. **15**, 6608 (2013).

[12] F. Brivio, J. M. Frost, J. M. Skelton, A. J. Jackson, O. J. Weber, M. T. Weller, A. R. Goñi, A. M. A. Leguy, P. R. F. Barnes, and A. Walsh, Lattice dynamics and vibrational spectra of the orthorhombic, tetragonal, and cubic phases of methylammonium lead iodide, Phys. Rev. B **92**, 144308 (2015).

[13] G. R. Medders and F. Paesani, Infrared and Raman spectroscopy of liquid water through “first-principles” many-body molecular dynamics, J. Chem. Theor. Comput. **11**, 1145 (2015).

[14] S. Y. Willow, M. A. Salim, K. S. Kim, and S. Hirata, *Ab initio* molecular dynamics of liquid water using embedded-fragment second-order many-body perturbation theory towards its accurate property prediction, Sci. Rep. **5**, 1 (2015).

[15] A. L. Brayton, I. C. Yeh, J. W. Andzelm, and G. C. Rutledge, Vibrational analysis of semicrystalline polyethylene using molecular dynamics simulation, Macromolecules **50**, 6690 (2017).

[16] D. R. Roe and T. E. Cheatham, PTRAJ and CPPTRAJ: Software for processing and analysis of molecular dynamics trajectory data, J. Chem. Theory Comput. **9**, 3084 (2013).

[17] A. Papoulis, *The Fourier Integral and Its Applications* (McGraw-Hill, New York, 1962).

[18] J. Matsui, T. Odagaki, and Y. Hiwatari, Study of the Slow Dynamics in a Highly Supercooled Fluid: Superlong-Time Molecular-Dynamics Calculation of the Generalized Susceptibility, Phys. Rev. Lett. **73**, 2452 (1994).

[19] J. Matsui, H. Miyagawa, T. Muranaka, K. Uehara, T. Odagaki, and Y. Hiwatari, Calculation of the generalized susceptibility for a highly supercooled fluid through molecular-dynamics simulation, Mol. Simul. **12**, 305 (1994).

[20] J. Matsui and Y. Hiwatari, Time autocorrelation function of intramolecular dipole moments for type-A polymer glass, J. Phys. Soc. Jpn. **74**, 2849 (2005).

[21] J. P. Hansen and I. R. McDonald, *Theory of Simple Liquids: With Applications to Soft Matter*, 4th ed. (Elsevier, Amsterdam, 2013).

[22] K. S. Cole and R. H. Cole, Dispersion and absorption in dielectrics I. Alternating current characteristics, J. Chem. Phys. **9**, 341 (1941).

[23] G. Strobl, *The Physics of Polymers Concepts for Undertanding Their Structure and Behavior*, 2nd ed. (Springer, Berlin, 2013).

[24] L. Van Hove, Correlations in space and time and Born approximation scattering in systems of interacting particles, Phys. Rev. **95**, 249 (1954).

[25] U. Buchenau, N. Nücker, and A. J. Dianoux, Neutron Scattering Study of the Low-Frequency Vibrations in Vitreous Silica, Phys. Rev. Lett. **53**, 2316 (1984).

[26] V. Malinovsky and A. Sokolov, The nature of boson peak in Raman scattering in glasses, Solid State Commun. **57**, 757 (1986).

[27] T. Kanaya, K. Kaji, S. Ikeda, and K. Inoue, Low-energy excitations in polyethylene: Comparison between amorphous and crystalline phases, Chem. Phys. Lett. **150**, 334 (1988).

[28] R. Zorn, A. Arbe, J. Colmenero, B. Frick, D. Richter, and U. Buchenau, Neutron scattering study of the picosecond dynamics of polybutadiene and polyisoprene, Phys. Rev. E **52**, 781 (1995).

[29] B. Frick and D. Richter, The microscopic basis of the glass transition in polymers from neutron scattering studies, Science **267**, 1939 (1995).

[30] O. Yamamuro, T. Matsuo, K. Takeda, T. Kanaya, T. Kawaguchi, and K. Kaji, Inelastic neutron scattering study of low energy excitations in glassy 1-butene, J. Chem. Phys. **105**, 732 (1996).

[31] I. Tsukushi, T. Kanaya, and K. Kaji, Spatial scale of low-energy excitation in amorphous polymers, J. Non-Cryst. Solids **235–237**, 250 (1998).

[32] R. J. Roe, Short time dynamics of polymer liquid and glass studied by molecular dynamics simulation, J. Chem. Phys. **100**, 1610 (1994).

[33] G. Ruocco and F. Sette, High-frequency vibrational dynamics in glasses, J. Phys.: Condens. Matter **13**, 9141 (2001).

[34] H. Shintani and H. Tanaka, Universal link between the boson peak and transverse phonons in glass, Nat. Mater. **7**, 870 (2008).

[35] A. Koyama, T. Yamamoto, K. Fukao, and Y. Miyamoto, Molecular dynamics studies on local ordering in amorphous polyethylene, J. Chem. Phys. **115**, 560 (2001).

[36] D. Rigby and R. J. Roe, Molecular dynamics simulation of polymer liquid and glass. I. Glass transition, J. Chem. Phys. **87**, 7285 (1987).

[37] T. Yamamoto, Monte Carlo simulation of the crystal structure of the rotator phase of *n*-araffins, J. Chem. Phys. **82**, 3790 (1985).

[38] T. Yamamoto, Monte Carlo simulation of the crystal structure of the rotator phase of *n*-paraffins. II. Effects of rotation and translation of the rigid molecules, J. Chem. Phys. **89**, 2356 (1988).

[39] K. Nozaki, N. Higashitani, T. Yamamoto, and T. Hara, Solid-solid phase transitions in *n*-alkanes $C_{23}H_{48}$ and $C_{25}H_{52}$: X-ray power diffraction study on new layer stacking in phase V, J. Chem. Phys. **103**, 5762 (1995).

[40] K. Nozaki, T. Yamamoto, T. Hara, and M. Hikosaka, Rotator phase transition through an intermediate state in odd *n*-alkanes: *In situ* optical observation study, Jpn. J. App. Phys. **36**, L146 (1997).

[41] T. Phillips and S. Hanna, A comparison of computer models for the simulation of crystalline polyethylene and the long *n*-alkanes, Polymer **46**, 11003 (2005).

[42] N. Wentzel and S. T. Milner, Crystal and rotator phases of *n*-alkanes: A molecular dynamics study, J. Chem. Phys. **132**, 044901 (2010).

[43] J. D. Barnes, Inelastic neutron scattering study of the "rotator" phase transition in *n*-nonadecane, J. Chem. Phys. **58**, 5193 (1973).

[44] M. Maroncelli, S. P. Qi, H. L. Strauss, and R. G. Snyder, Nonplanar conformers and the phase behavior of solid *n*-alkanes, J. Am. Chem. Soc. **104**, 6237 (1982).

[45] G. Ungar, Structure of rotator phases in *n*-alkanes, J. Phys. Chem. **87**, 689 (1983).

[46] J. Doucet and A. J. Dianoux, Rotational diffusion in the rotator phase of *n*-alkanes, J. Chem. Phys. **81**, 5043 (1984).

[47] J.-P. Ryckaert and M. L. Klein, Translational and rotational disorder in solid *n*-alkanes: Constant temperature-constant pressure molecular dynamics calculations using infinitely long flexible chains, J. Chem. Phys. **85**, 1613 (1986).

[48] E. Helfand, Transport coefficients from dissipation in a canonical ensemble, Phys. Rev. **119**, 1 (1960).

[49] W. G. Hoover, D. J. Evans, R. B. Hickman, A. J. C. Ladd, W. T. Ashurst, and B. Moran, Lennard-Jones triple-point bulk and shear viscosities. Green-Kubo theory, Hamiltonian mechanics, and nonequilibrium molecular dynamics, Phys. Rev. A **22**, 1690 (1980).

[50] F. L. Galeener and P. N. Sen, Theory for the first-order vibrational spectra of disordered solids, Phys. Rev. B **17**, 1928 (1978).

[51] J. R. Ferraro, K. Nakamoto, and C. W. Brown, *Introductory Raman Spectroscopy*, 2nd ed. (Elsevier, Amsterdam, 2003), pp. 1–434.

[52] A. Strachan, Normal modes and frequencies from covariances in molecular dynamics or Monte Carlo simulations, J. Chem. Phys. **120**, 1 (2004).

[53] K. Fukao and Y. Miyamoto, Glass transitions and dynamics in thin polymer films: Dielectric relaxation of thin films of polystyrene, Phys. Rev. E **61**, 1743 (2000).

[54] F. A. Morrison, *Understanding Rheology* (Oxford University Press, Oxford, 2001), p. 545.

[55] M. Andreev and G. C. Rutledge, A slip-link model for rheology of entangled polymer melts with crystallization, J. Rheol. **64**, 213 (2020).

[56] J. Ramírez, S. K. Sukumaran, B. Vorselaars, and A. E. Likhtman, Efficient on the fly calculation of time correlation functions in computer simulations, J. Chem. Phys. **133**, 154103 (2010).

[57] H. J. Berendsen, J. P. Postma, W. F. Van Gunsteren, A. Dinola, and J. R. Haak, Molecular dynamics with coupling to an external bath, J. Chem. Phys. **81**, 3684 (1984).

[58] S. Nosé, A unified formulation of the constant temperature molecular dynamics methods, J. Chem. Phys. **81**, 511 (1984).

[59] W. G. Hoover, Canonical dynamics: Equilibrium phase-space distributions, Phys. Rev. A **31**, 1695 (1985).

[60] H. C. Andersen, Molecular dynamics simulations at constant pressure and/or temperature, J. Chem. Phys. **72**, 2384 (1980).

[61] M. Mondello and G. S. Grest, Molecular dynamics of linear and branched alkanes, J. Chem. Phys. **103**, 7156 (1995).

[62] D. N. Theodorou and U. W. Suter, Detailed molecular structure of a vinyl polymer glass, Macromol. **18**, 1467 (1985).

[63] G. Tarjus, S. A. Kivelson, Z. Nussinov, and P. Viot, The frustration-based approach of supercooled liquids and the glass transition: A review and critical assessment, J. Phys.: Condens. Matter **17**, R1143 (2005).

[64] H. Shintani and H. Tanaka, Frustration on the way to crystallization in glass, Nat. Phys. **2**, 200 (2006).

[65] F. Y. Hansen, J. C. Newton, and H. Taub, Molecular dynamics studies of the melting of butane and hexane monolayers adsorbed on the basal-plane surface of graphite, J. Chem. Phys. **98**, 4128 (1993).

[66] F. Y. Hansen, K. W. Herwig, B. Matthies, and H. Taub, Intramolecular and Lattice Melting in *n*-Alkane Monolayers: An Analog of Melting in Lipid Bilayers, Phys. Rev. Lett. **83**, 2362 (1999).